



# Analogue computing with metamaterials

Farzad Zangeneh-Nejad<sup>1</sup>, Dimitrios L. Sounas<sup>2</sup>, Andrea Alù<sup>3</sup> and Romain Fleury<sup>1</sup>

**Abstract** | Despite their widespread use for performing advanced computational tasks, digital signal processors suffer from several restrictions, including low speed, high power consumption and complexity, caused by costly analogue-to-digital converters. For this reason, there has recently been a surge of interest in performing wave-based analogue computations that avoid analogue-to-digital conversion and allow massively parallel operation. In particular, novel schemes for wave-based analogue computing have been proposed based on artificially engineered photonic structures, that is, metamaterials. Such kinds of computing systems, referred to as computational metamaterials, can be as fast as the speed of light and as small as its wavelength, yet, impart complex mathematical operations on an incoming wave packet or even provide solutions to integro-differential equations. These much-sought features promise to enable a new generation of ultra-fast, compact and efficient processing and computing hardware based on light-wave propagation. In this Review, we discuss recent advances in the field of computational metamaterials, surveying the state-of-the-art metastructures proposed to perform analogue computation. We further describe some of the most exciting applications suggested for these computing systems, including image processing, edge detection, equation solving and machine learning. Finally, we provide an outlook for the possible directions and the key problems for future research.

Nowadays, digital signal processors (DSPs) are ubiquitously used to carry out a wide variety of computational tasks, from relatively simple to highly complex ones<sup>1</sup>. DSPs generally consist of three basic components: an analogue-to-digital converter (A/D), a processing unit and, often, a digital-to-analogue converter (D/A). The first sub-block (A/D) takes an analogue signal (representing, for instance, an image or voice) and discretizes it into a series of bits. The second sub-block, the processing unit, manipulates the discretized version of the analogue signal according to the desired computational operation. The resulting digital stream can then be converted back into the analogue domain using the D/A sub-block.

Despite their versatile functionality, DSPs have several drawbacks, most of which arise from the unavoidable analogue-to-digital conversion. In particular, the A/D and D/A sub-blocks of DSPs tend to consume significant power. This renders DSPs cost-inefficient, especially when it comes to performing simple computational tasks such as differentiation or integration<sup>2</sup>. The A/D and D/A converters also restrict the speed of processing, given that the discretization process is time-consuming and cannot be performed in a massively parallel manner. Moreover, at high frequencies (above the GHz range), the A/D and D/A converters fail

to perform discretization properly because the signals vary too rapidly. These limitations have led to a surge of interest in revisiting the idea of analogue computing, which may be traced back to several decades ago, in which signal processing happens in the analogue domain and, hence, the analogue-to-digital conversion is not needed.

An analogue computer is a device that takes advantage of continuous variations in a given physical phenomenon to perform a certain computational or processing task. The first electronic or mechanical analogue computers, originally preferred to digital versions, were based on continuously varying quantities, such as electric current or mechanical motion<sup>3</sup> (BOX 1). Despite being free of A/D and D/A converters, such kinds of computers turned out to be very slow and bulky, hindering their applicability in modern systems, in which high speed and miniaturization are sought. In addition, small errors triggered by noise were found to propagate and be amplified, as the signals were processed in series. Digital computers could overcome these challenges, and took over the scene.

Recently, the interest in analogue computing was revived in the context of metamaterials research, as it was shown that subwavelength structures could

<sup>1</sup>Laboratory of Wave Engineering, School of Electrical Engineering, Swiss Federal Institute of Technology in Lausanne (EPFL), Lausanne, Switzerland.

<sup>2</sup>Department of Electrical Engineering, Wayne State University, Detroit, MI, USA.

<sup>3</sup>Photonics Initiative, Advanced Science Research Center, City University of New York, New York, NY, USA.

e-mail: [romain.fleury@epfl.ch](mailto:romain.fleury@epfl.ch)

<https://doi.org/10.1038/s41578-020-00243-2>

implement computing functionalities by leveraging light propagation in suitably engineered artificial photonic materials<sup>4</sup>. This solution enables ultra-fast speeds, low loss, subwavelength form factors and massively parallel operations, holding the promise to overcome the aforementioned challenges. This computing

platform is indeed based on the enhanced interaction of optical fields with artificially created structures, the metamaterials<sup>5–18</sup>. As opposed to conventional electronic and mechanical computers, computational photonic metamaterials can be very fast. This is because they operate at the speed of light and, more importantly, are

#### Box 1 | History of analogue computing

The earliest known analogue computer, invented in Greece between 150 and 100 BC, is the Antikythera mechanism<sup>135,136</sup>, intended for specific astronomical applications (see the figure, panel a). The device was composed of nearly 40 gears and wheels, and was devised to model the position of the Moon and the Sun in their orbits, providing the possibility of predicting eclipses.

Similar mechanical analogue computers were later developed for astronomical purposes. A prominent, more recent example of such a device is the astronomical clock<sup>137</sup> that appeared in the 14th century, which was capable of analysing complex astronomical phenomena, such as the relative positions of the Earth, Sun, Moon and planets.

Mechanical analogue computers have also been used for computational purposes other than astronomical calculations. One of the mechanical computing devices commonly used since the 17th century were slide rules<sup>138</sup>, performing multiplications and divisions<sup>139</sup> (see the figure, panel b).

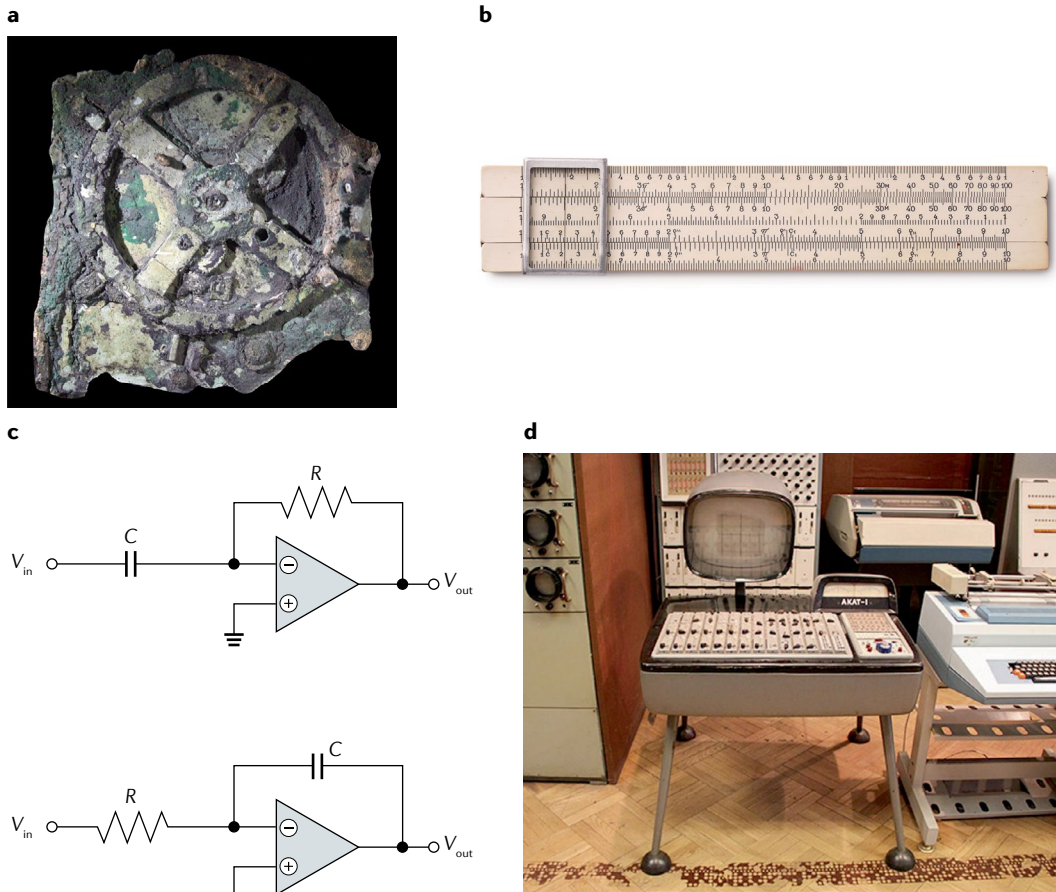
Such kinds of computers, developed shortly after the description of logarithms, worked based on the fact that the multiplication (or division) of two real numbers can be expressed as the addition (or subtraction) of their logarithms.

Before the introduction of portable electronic computers, many other mechanical computers were developed. Examples include: the planimeter, used to calculate the area within a closed 2D shape<sup>139</sup>; the tide predictor<sup>140</sup> (developed in 1878), a mechanical analogue computer predicting the behaviour of sea tides; the Dumaresq<sup>135</sup>, an analogue computer developed in 1902 to relate the parameters of fire-control systems to the ones of a moving target object; the nomograph<sup>141</sup> (invented in 1918), a special mechanical equation solver solving a specific class of equations having the form  $f(x,y,z)=0$ ; and the differential analyser<sup>135</sup> (invented in 1930), which could solve second-order and higher-order differential equations.

Despite their simple principle of operation, mechanical analogue computers suffer from several restrictions, including their large size and high production cost. Driven by advances in electronics, electronic analogue computers emerged. The underlying principle of electronic analogue computers is that, by engineering the connectivity between the circuit elements, the transfer function of a circuit can be tailored to follow that of a mathematical operation. The top part of the figure, panel c, for example, represents an electronic circuit realizing the operator of first-order differentiation. By employing simple circuit-analysis techniques, the transfer function of the circuit can be found as  $V_{\text{out}}/V_{\text{in}} = i\omega RC$  (where  $V_{\text{out}}$  is the output voltage,  $V_{\text{in}}$  the input voltage,  $\omega$  the frequency,  $R$  the resistance and  $C$  the capacitance). In the time domain, the relation between  $V_{\text{out}}$  and  $V_{\text{in}}$  is expressed as  $V_{\text{out}} = -RCdV_{\text{in}}/dt$ , indicating that the circuit acts as a first-order differentiator. The bottom part of panel c illustrates another electronic circuit, which acts as an analogue integrator.

The first generation of electronic analogue computers was developed in the middle of 20th century. For example, the computer shown in the figure, panel d, called AKAT-1, was composed of several operational amplifiers, transistors and regular passive elements. The system, developed in 1959, was designed to address complex dynamic processes, such as heat transfer, by analysing the associated differential equations. Compared with their mechanical ancestors, electronic analogue computers were much faster and smaller, and could be adapted to a wider range of analogue functionalities. Their early adoption was abandoned in favour of digital computers, which were more robust to noise.

Figure, panel a, image from CPA Media Pte Ltd/Alamy Stock Photo; panel b, image from Anton Starikov/Alamy Stock Photo; panel d, image courtesy Tablet magazine.



capable of performing a large number of operations in parallel. At the same time, the very small wavelength of optical waves enables miniaturization and integration. These features, hence, create the ideal conditions for carrying out specific-purpose signal-processing tasks with ultra-fast speed and massive parallelization, at scales potentially smaller than the wavelength.

In this Review, we discuss recent advances in this thriving area of research. We start by describing different approaches proposed for wave-based analogue computing, including the Fourier optics approach<sup>19,20</sup>, the Green's function metamaterial approach<sup>4</sup> and the metasurface approach<sup>4</sup>. We then outline the designs and unusual properties of state-of-the-art computational metamaterials, proposed in various areas of wave physics, such as photonics and phononics. Afterwards, we discuss recent developments and applications of computational metamaterials in modern engineering, such as equation solving, machine learning and topological analogue signal processing. In the last part of the Review, we provide an outlook for possible future directions, including multifunctional computational metamaterials, intelligent metamaterial computing systems and wave-based analogue signal processors based on disorder.

### Analogue computing principles

#### Fourier optics

**Principle of operation.** The idea of leveraging waves to perform analogue computing dates back to several decades before the development of computational metamaterials. In fact, a simple (convex) lens acts as a Fourier transformer on an image placed in its focal plane<sup>19–22</sup>, transforming a constant illumination, in the form of a uniform, monochromatic plane-wave incident field with planes of constant phase perpendicular to the lens axis, into a single dot at its focal length, which approaches a delta Kronecker function in the limit of a lens with infinite aperture. Conversely, the emission from a point-like source is ideally converted into a uniform plane wave by the lens. The ability of lenses to take the Fourier transform of incident fields is at the basis of Fourier optics, which is the simplest example of a platform for using light to perform signal-processing tasks.

The general principle of Fourier optics is to convert a signal to the Fourier space, perform the signal-processing operation on the Fourier-transformed signal and then convert the output back to the regular space. As an example, let us suppose that an arbitrary image is placed in the front focal plane of an optical lens. At the back focal plane of the lens, the 2D spatial Fourier transform of the corresponding image is generated. At this plane, the spectral features of the image can be manipulated using a mask plate with a specific transverse transparency pattern. If, for instance, we cover the centre of the Fourier plane with an opaque mask plate, and then use a second lens to inverse-Fourier-transform the image, the low-order Fourier components will be suppressed, but the information associated with the higher-order harmonics will be maintained, enhancing the edges. Similarly, a pinhole mask placed at the centre of the Fourier plane attenuates the information associated with the high-order Fourier components, blurring

the edges of the image and keeping its slower variations. This optical system, known as a 4F correlator<sup>19</sup> (the name comes from the fact that the system is four focal lengths long), can, therefore, apply a large number of linear operations to the Fourier spectrum of an image. The science of Fourier optics, indeed, consists in tailoring the local transmission amplitude and phases of the Fourier mask to achieve various advanced functions.

Compared with conventional electronic analogue computers (BOX 1), analogue signal processors based on Fourier optics are much faster, because the speed of light is much larger than the drift velocity of electrons. Yet, their bulky structures, involving at least four focal lengths, broadly hinder their miniaturization. Alignment issues and aberrations caused by the realistic features of the lenses further complicate the picture. Despite all of these challenges, Fourier optics is a well-established field of science and technology<sup>19</sup>.

Electromagnetic metamaterials, compound materials made of artificial scatterers designed to achieve desired macroscopic properties, and their 2D versions, electromagnetic metasurfaces, can shrink dramatically the size of these processing systems and avoid the need for Fourier-transforming the image twice. Like analogue signal processors based on Fourier lenses, metamaterial computing systems can be superfast (because they are based on propagating waves). However, as opposed to conventional Fourier optics signal processors, computational metamaterials and metasurfaces can be made smaller than the operation wavelength, because they usually rely on subwavelength resonant scatterers. Two approaches have been introduced to computational metamaterials: the Green's function approach and the metasurface approach, as detailed in the following.

#### Green's function approach

**Principle.** The Green's function method<sup>4,23–38</sup> has guided several designs of metamaterial computing systems. As the name of the method denotes, in the Green's function approach, the Green's function of the operator of choice is directly realized in real space, without transforming back and forth from the spatial to the spectral domain, gaining in compactness and avoiding possible challenges in error propagation and alignment issues. Let us consider a hypothetical linear system (FIG. 1a), which acts on an input signal  $f$  and turns it into the output  $g$ . The signals  $f$  and  $g$  could be, for example, the optical fields that are incident on and transmitted through a metamaterial. For simplicity, we assume here that the fields only vary with respect to a single spatial coordinate  $y$ . Because our system should apply an operation on this incoming 1D function independent of its specific  $y$  variations, we require that the metamaterial properties are invariant upon translations along  $y$ , whereas the input and output signals,  $f(y)$  and  $g(y)$ , explicitly depend on  $y$ . From a system theory point of view,  $f(y)$  and  $g(y)$  are related to each other through the Green's function of the metamaterial, defined in the Fourier space as  $H(k_y) = \text{FT}[g(y)]/\text{FT}[f(y)]$ , in which FT stands for the Fourier transform. By engineering the metamaterial properties, we can actually tailor the associated Green's function  $H(k_y)$  to match the transfer function of the desired operator.

This design can be performed either by direct optimization or by inverse design, using, for instance, generalized sheet transition conditions<sup>39</sup> in the case of metasurface design. To provide a concrete example, let us consider the irregularly shaped transfer function  $H_0(k_y)$ , whose amplitude is shown in FIG. 1b. The transfer function is associated with an arbitrarily chosen mathematical operation. The Green's function method can be employed to implement this transfer function in a composite metamaterial, for instance, the multilayered structure shown in FIG. 1c,

composed by a stack of subwavelength metamaterial slabs. Each layer has a specific thickness ( $d_i$ ), permittivity ( $\epsilon_i$ ) and permeability ( $\mu_i$ ). By running an optimization on the parameters  $d_i$ ,  $\epsilon_i$  and  $\mu_i$ , it is possible to make the Green's function of the multilayered structure to be approximately equal to the transfer function of the operator of choice, that is,  $H_0(k_y)$ . In this case, in real space, the optimized metamaterial acts as an analogue signal processor, applying the desired mathematical operation in the spatial domain to any incident signal  $f(y)$ .

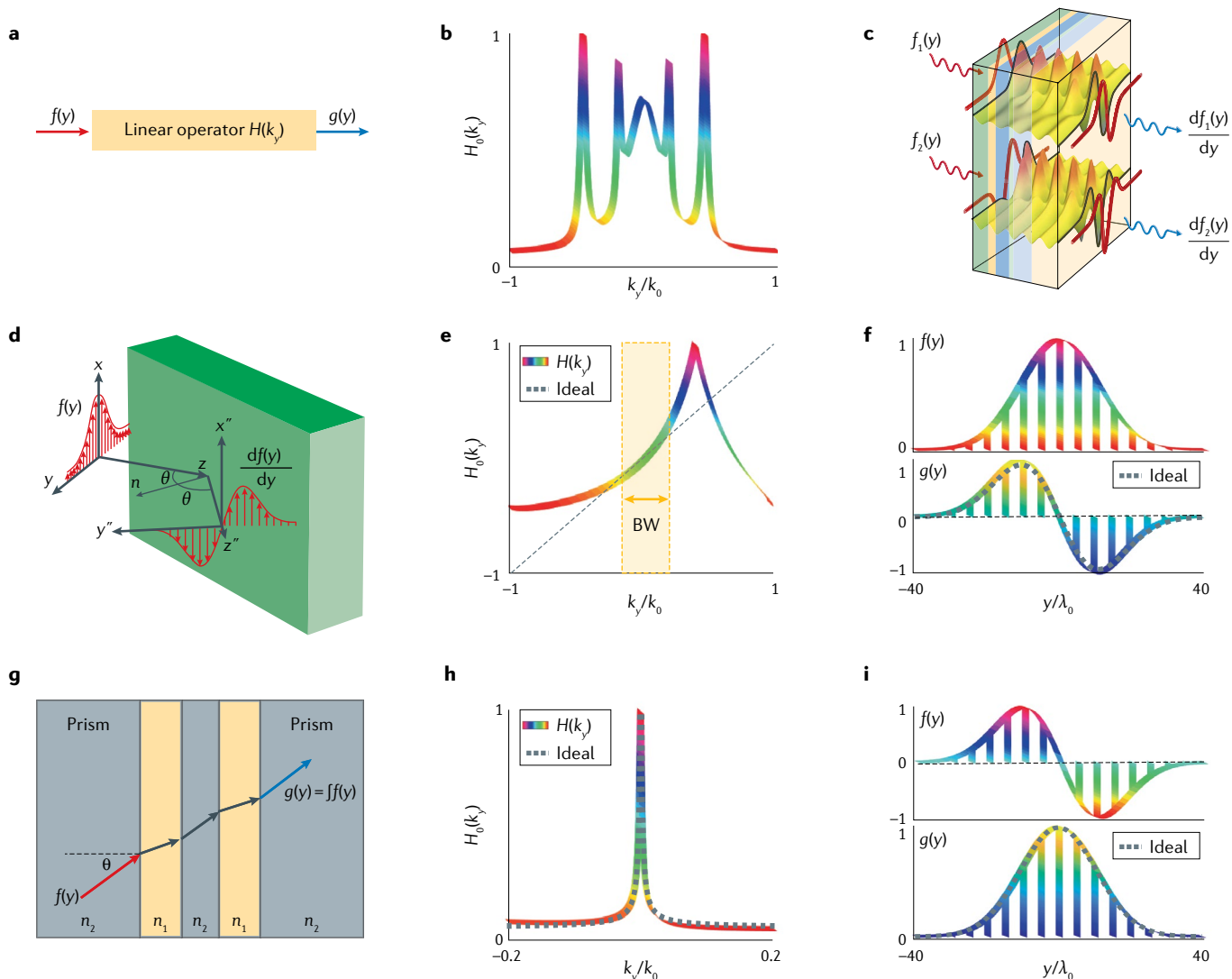


**Fig. 1 | Wave-based analogue computing based on the Green's function approach.** **a** | A hypothetical analogue computing system characterized by the Green's function  $H(k_y)$ . **b** | Transfer function (amplitude) of an arbitrary linear operator to be realized using the Green's function method. **c** | Example of a computational metamaterial based on the Green's function method. The metamaterial consists of multilayered dielectric slabs. By optimizing the permittivity, permeability and thickness of each slab, it is possible to engineer the Green's function of the structure such that it matches the desired transfer function,  $H_0(k_y)$ . **d** | Analogue spatial differentiator based on the Green's function method. The differentiator consists only of an interface between a dielectric and free space, on which a transverse-magnetic-polarized incident beam impinges at the Brewster angle. **e** | Green's function (reflection spectrum) of the Brewster differentiator near the Brewster angle. For sufficiently wide incident signals with bandwidth (BW) within the yellow

region, the Green's function can be approximated with a linear function (the dashed line), following the transfer function of the ideal differentiator. **f** | Corresponding differentiated reflected field (bottom panel) when the interface is illuminated with a Gaussian incident field (top panel). **g** | An analogue spatial integrator, based on resonant tunnelling through a dielectric slab waveguide.  $n_1$  and  $n_2$  are the refractive indices of the core and cladding layers, respectively. **h** | At a specific incident angle, the momentum of the incident field matches the one of the guided mode, leading to a resonant tunnelling peak in the transmission spectrum of the structure. The spectral line shape of this resonance peak is the same as the one of an ideal integrator (the dashed line). **i** | Demonstration of the operation of the integrator. Panel **c** is adapted with permission from REF.<sup>4</sup>, AAAS. Panels **d–f** adapted with permission from REF.<sup>40</sup>, © The Optical Society. Panels **g** and **h** adapted with permission from REF.<sup>42</sup>, © The Optical Society.

**Implementation.** The Green's function method has been used to perform specific-purpose computing operations in recent years. One of the most popular mathematical operations implemented using this method, which is commonly used to determine sharp variations, edges and extremal values of signals, is differentiation. A simple optical structure that can be used to calculate the derivative of incident waves under certain conditions<sup>40</sup> is shown in FIG. 1d. This basic differentiator consists of an interface between two dielectrics with different refractive indices ( $n_1 = 1$  and  $n_2 = 3.4$ ). A transverse-magnetic (TM)-polarized incident field impinges on the interface. The TM Fresnel reflection coefficient of the interface for the incident angle  $\theta$  is expressed as

$$R(\theta) = \frac{n_1\sqrt{1 - (n_1/n_2 \sin \theta)^2} - n_2 \cos \theta}{n_1\sqrt{1 - (n_1/n_2 \sin \theta)^2} + n_2 \cos \theta}. \quad (1)$$

At the incident angle  $\theta_B = \tan^{-1}(n_2/n_1)$ , known as the Brewster angle<sup>41</sup>, the TM reflection coefficient of the structure vanishes: this is the case represented in FIG. 1d. It is easy to verify that the relation between the Brewster angle, the angular parameter  $\theta$  and the wavenumber  $k_y$  is

$$k_y = k_0 \sin(\theta - \theta_B) \quad (2)$$

in which  $\theta$  varies between 0 and  $\pi/2$ . Note that the coordinate system for the signal is not aligned with the interface, as represented in FIG. 1d. Equation 2 defines a one-to-one mapping between the angular parameter  $\theta$  and the wavenumber  $k_y$ , based on which the Fresnel reflection coefficient of Eq. 1 can be transformed into the spatial Fourier domain. The corresponding spatial Fourier spectrum of the Fresnel reflection coefficient around the Brewster angle is shown in FIG. 1e. As observed, the reflection spectrum of the interface becomes equal to zero at  $k_y = 0$  (note that this wavenumber corresponds to  $\theta = \theta_B$ , Eq. 2). Near this zero, the reflection spectrum can be approximated with a linear function of the form  $R(k_y) \approx Ak_y$  (Taylor expansion), in which  $A = -(n_2/2 - 1/2n_2^3)/k_0$  (the slope of the dashed line in FIG. 1e). Interestingly,  $R(k_y)$  is very similar to the Green's function of the ideal spatial differentiator, namely,  $H(k_y) = ik_y$ , other than a proportionality coefficient. This implies that, for signals impinging on the interface at the Brewster angle with a sufficiently narrow spatial spectrum around that angle (the yellow-shaded region in FIG. 1e), the reflected field is the derivative of the incident field. This is demonstrated in FIG. 1f, in which the reflected field ( $g(y)$ , bottom panel) corresponding to a Gaussian incident signal ( $f(y)$ , top panel) is shown.  $g(y)$  has a Gaussian derivative profile, evidencing the proper operation of a differentiator, assuming that the image does not have too large spectral features. It should be noted that, because the differentiator works near a zero of reflection, the amplitude of the derivative signal (the reflected field) is generally small, leading to relatively low signal-to-noise ratio. This property is inherent to the derivative operation.

A similar approach can be used to perform analogue integration<sup>42</sup>: consider the configuration shown

in FIG. 1g, the well-known dielectric slab waveguide geometry, whose core and cladding layers have refractive indices of  $n_2 = 3.4$  and  $n_1 = 1.5$ , respectively. The structure is excited from the far field using a prism coupler at incident angle  $\theta$ . At some specific  $\theta$ , the transverse momentum of the incoming beam  $f(y)$  becomes equal to the one of the guided mode of the slab waveguide, leading to a resonance peak in the transmission spectrum (FIG. 1h). Around this resonance, we can approximate the transmission coefficient of the system with  $T(k_y) = A/k_y$ , in which  $A$  is a constant depending on the quality factor of the resonance. This approximation is acceptable only for signals that satisfy two conditions: first, the incident field must have a sufficiently small spectral bandwidth, because, away from the transparency condition, the transmission is zero and no output is generated. Second, the incident field must only possess non-zero spatial-frequency components. Indeed, integrating a signal with a non-zero spatial-frequency component requires amplifying the output, because the transfer function of the ideal integrator  $T(k_y) = A/k_y$  blows up at  $k_y = 0$ . Such operation is, therefore, impossible in a passive device for which the transmission is always below one, unless one only works with signals without any component at  $k_y = 0$ . Under these conditions,  $T(k_y)$  is similar, up to a constant factor, to the transfer function of the ideal integrator ( $G(k_y) = 1/ik_y$ ). Hence, such a simple structure functions like an analogue integrator. This is illustrated in FIG. 1i, which shows the transmitted field (bottom panel) corresponding to a Gaussian derivative incident signal (which, indeed, has no zero-spatial-frequency component, top panel). As expected, the transmitted field has a Gaussian profile. We note that the structures in FIG. 1d,g are not metamaterials per se and, as such, cannot be used for realizing arbitrarily complex computing operations. Yet, these examples provide an intuitive idea of the underlying principle of the Green's function method, which is directly applicable to metamaterial platforms.

The described analogue differentiator and integrator can be employed as building blocks to construct more complex analogue operations. Suppose, for instance, that we want to realize an analogue second-order differentiator. This can be readily accomplished by cascading two realizations of first-order differentiators, each of which differentiates the incident signal one time. Similarly, a second-order integrator can be realized by cascading two first-order integrators. We stress that these two practical examples are limited in the extent of images that can be processed (only images with slow variations impinging from specific angles) and in the overall efficiency of the output. Yet, the general platform used for the Green's function method, as in FIG. 1c, in which optimized multilayers can arbitrarily tailor the Green's function output  $H(k_y)$ , hold the promise to implement more sophisticated and efficient analogue processing metamaterials.

**Examples and applications.** The applicability of the Green's function method for performing wave-based analogue computing has been experimentally verified

in a series of proposals. In a first example, somewhat analogous to the implementation in FIG. 1d, an analogue spatial differentiator based on the resonance behaviour of surface plasmon polaritons (SPPs) was experimentally demonstrated<sup>43</sup>. The differentiator, shown in FIG. 2a, includes a thin layer of metallic film and a prism coupler. At the incident angle at which the momentum of the excitation field matches the one of the SPP mode (phase-matching condition), the reflection spectrum drops to zero (FIG. 2b). Around this dip, the reflection

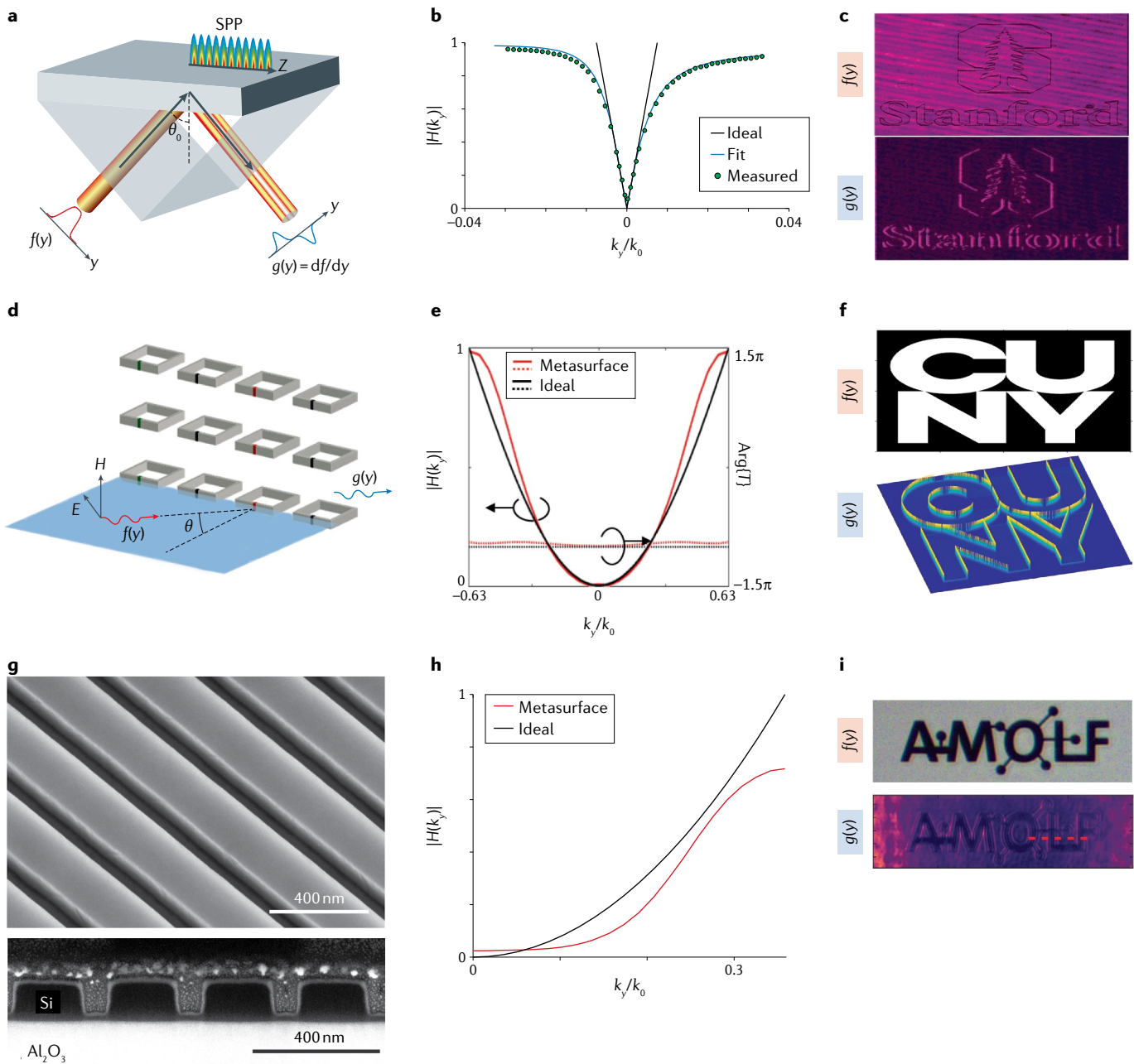


**Fig. 2 | Analogue computing systems based on the Green's function method.** **a** | A spatial analogue differentiator based on a thin metallic film supporting surface plasmon polaritons (SPPs). **b** | Green's function of the structure (the reflection spectrum) near  $k_y=0$ , showing a resonance dip (zero). Near this zero, the Green's function can be approximated with a linearly varying function (the straight lines), corresponding to the transfer function of the ideal differentiator. **c** | Spatial edge detection based on the plasmonic spatial differentiator shown in panel a. **d** | Spatial differentiation based on a metasurface array composed of split-ring resonators. The refractive indices of the dielectrics inside the SPP gaps are modulated with a slowly varying function, offering a degree of freedom to enhance the operation spectral bandwidth and the overall efficiency. **e** | Magnitude

(solid line, left vertical axis) and phase (dashed line, right vertical axis) of the Green's function of the structure in panel d, agreeing well with the one of an ideal differentiator. **f** | Spatial edge detection based on the metasurface array shown in panel d. **g** | Scanning electron microscope image (top and side view) of an optical computing metasurface engineered such that it realizes the transfer function for second-order differentiation. **h** | Transfer function of the metasurface. **i** | Edge detection based on the metasurface shown in panel g. Panels a–c adapted from REF.<sup>43</sup>, CC BY 4.0. Panels d–f adapted with permission from REF.<sup>46</sup>, APS. Panels g–i with permission from REF.<sup>47</sup>, <https://pub.acs.org/doi/10.1021/acs.nanolett.9b02477>, further permission related to the material excerpted should be directed to the ACS.

spectrum follows the transfer function of a first-order differentiator (the straight lines). The fact that this differentiator is only composed of a single metallic layer makes the fabrication of the system simple. In addition, it represents a significant miniaturization compared with signal processors based on conventional bulky Fourier elements. At the same time, its operation is limited to a narrow spatial spectrum around the dip in reflection and does not avoid the aforementioned limitations in terms of overall resolution of the images that can be processed and of overall efficiency.

Several important applications have been proposed for analogue spatial differentiators. In one dimension, they can be used to determine the sharp variations of functions. Likewise, in two dimensions, spatial differentiation provides the possibility of detecting the sharp variations of incident images (2D signals), that is, their edges<sup>44,45</sup>. FIGURE 2c demonstrates the possibility of performing edge detection using the plasmonic spatial differentiator shown in FIG. 2a. To this end, the incident field was modulated with a spatial light modulator and projected onto the metal film of the plasmonic differentiator. The bottom panel of FIG. 2c depicts the corresponding reflected image. Indeed, the edges of the incident image (FIG. 2c, top) have been resolved. Note that the vertical edges of the image are resolved better, because the differentiation is performed only along the horizontal direction ( $y$  axis). Yet, as long as the edge is not purely vertical, its signature can be traced in the reflected image. This limitation was later overcome with a design based on all-dielectric metasurfaces<sup>22</sup>, which had the additional advantage of being less affected by absorption losses.

As mentioned above, as a trade-off for its simplicity, the plasmonic spatial differentiator has a few drawbacks. In particular, it works only for incident waves possessing a narrow spatial bandwidth (this is caused by the presence of higher-order terms in the Taylor series expansion of  $R(k_y)$ ). For this reason, the differentiator is not capable of resolving edges that are very close to each other. In a recent proposal<sup>46</sup>, a more sophisticated spatial analogue differentiator going beyond these limitations was presented. The structure of the differentiator, shown in FIG. 2d, exploits a spatially modulated resonant metasurface with a strong non-local response, a property that is often considered undesirable for other metasurface applications. The metasurface array is composed of resonant particles (split-ring resonators, SRRs, resonating at a frequency  $f_0 = 1.26$  Ghz), on which a TM-polarized wave is normally incident. A slow periodic modulation is applied to the relative permittivities of the dielectrics inside the SRR gaps, leading to the appearance of a leaky-wave resonance with controllable non-locality. At the leaky-wave-resonance frequency, the reflection coefficient of the structure drops to zero. Furthermore, this frequency is a function of the incident angle, owing to the non-local properties of the leaky wave. Then, if the operation frequency is equal to the leaky-wave frequency at normal incidence, the reflection spectrum changes as a function of the incident angle according to a parabolic function law, matching the transfer function of the second-order differentiator<sup>22,35</sup>. Interestingly, the

spatial modulation applied to the metasurface profile provides an additional degree of freedom to enhance the bandwidth of operation. More specifically, by precisely controlling the parameters of the modulation, the corresponding higher-order (above the third order) Taylor coefficients can be cancelled, allowing one to enhance the spatial bandwidth of differentiation, that is, the overall resolution of the device, and tune it to the desired level corresponding to the numerical aperture of the optical system of interest. The corresponding optimized Green's function, obtained using numerical simulations, is shown in FIG. 2e, and is in good agreement with the transfer function of the ideal case. The slight deviation from the ideal response might be suppressed by introducing more sophisticated modulation patterns over the metasurface profile. FIGURE 2f demonstrates the performance of this second-order differentiator for edge detection. Compared with the plasmonic spatial differentiator discussed earlier, this design provides a higher resolution for edge detection, thanks to its larger operational beamwidth. It is worth mentioning that it is also possible to achieve wideband first-order differentiation by slightly modifying the structure of FIG. 2d. To this end, one should break both the horizontal and vertical mirror symmetries of the system, for example, by adding a horizontally misplaced array structure on one side of the SRR array. Alternatively, the reflection symmetries of the structure can be broken by tilting the direction of the incident field, leading to a first-order zero around which the transmission follows a linearly varying function akin to the transfer function of the first-order differentiator.

The metasurface discussed above was designed to operate in the microwave range, but a similar response can be obtained at optical frequencies. An optical spatial differentiator based on a resonance-based metasurface array was realized<sup>47</sup>, composed of low-loss silicon dielectric resonators placed on top of an  $\text{Al}_2\text{O}_3$  substrate (FIG. 2g). By engineering the resonators composing the metasurface, the Green's function of the structure was tailored such that it approached the transfer function of the second-order derivative operator over a wide operational bandwidth (FIG. 2h). The excellent performance of this optical differentiator for characterizing the edges of incident images is demonstrated by the images in FIG. 2i. It should be noted that, although both the structures in FIG. 2d and in FIG. 2f work only for a specific polarization of the incident wave, a recent work has demonstrated the possibility of performing the same kinds of operation for both transverse-electric and TM polarizations<sup>48</sup>.

### Metasurface approach

**Principle.** Although the Green's function technique is a straightforward approach to realize specific-purpose computational functionalities, it does not generally provide a platform that can be easily adapted to an arbitrarily complex operator without using more complex geometries and optimization techniques. An alternative strategy, known as the metasurface approach<sup>49–68</sup>, has enabled the realization of a wider range of operators. The core idea of this approach, schematically sketched in FIG. 3a, is essentially to map the conventional 4F

correlator approach, commonly used in Fourier optics and described in the previous section, onto a more compact metamaterial platform. Consider a linear, shift-invariant system, aimed at applying a specific operator

(characterized by the transfer function  $H(k_x)$ ) to the input field  $f(x)$ . From a systems perspective, the relation between the input field  $f(x)$  and the corresponding output  $g(x)$  is expressed as

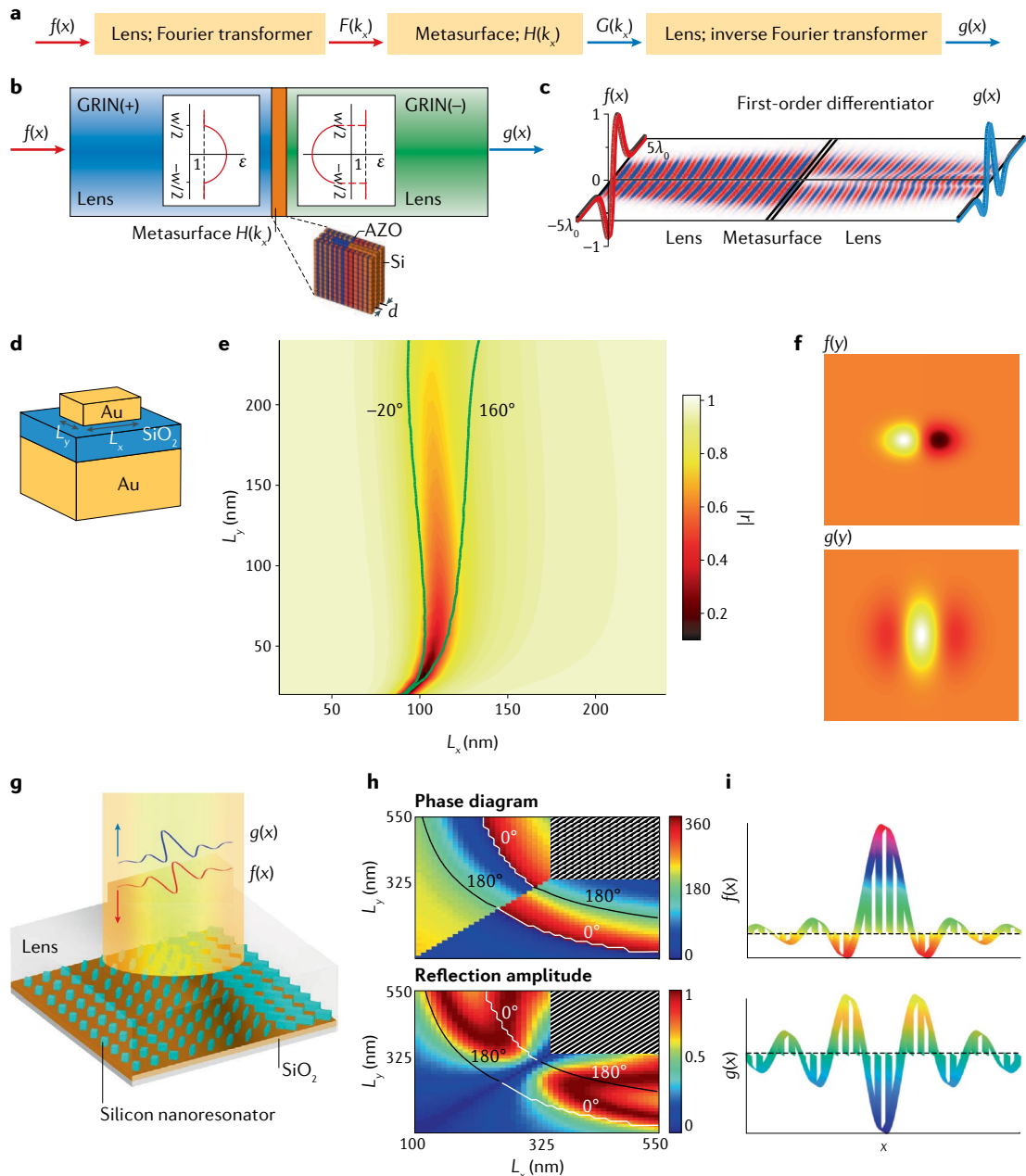


**Fig. 3 | Metasurface approach for wave-based analogue computing.** **a** Block diagram of a computing system based on the metasurface approach, consisting of three sub-blocks: two Fourier transformers (graded index (GRIN) and lenses) and a metasurface realizing the transfer function of the operator of choice. **b** A metasurface computing system designed to perform first-order differentiation. **c** First-order spatial differentiation based on the metasurface computing system in panel **b**. **d** Analogue computing based on a reflective metasurface array, consisting of silicon nanobricks arranged on a silica substrate and a thick metallic layer. **e** The amplitude and phase of the field reflected by the metasurface array can be manipulated independently by varying the length ( $L_x$ ) and width ( $L_y$ ) of the nanobricks. The plot shows the amplitude of the reflection coefficient,  $r$ . The green lines correspond to the phase of the reflection. **f** Experimental demonstration of the performance of the metasurface computing system in panel **d**. A Gaussian derivative incident field as the input field (top) results in a reflected field that is its derivative (bottom). **g** A dielectric metasurface computing system, consisting of silicon nanobricks deposited on top of a silica substrate. **h** Variation of the amplitude and phase of the reflection coefficient as a function of the length,  $L_x$ , and width,  $L_y$ , of the silicon nanobricks. **i** Demonstration of the operation of the metasurface computing system as a second-order spatial differentiator. Panels **b** and **c** adapted with permission from REF.<sup>4</sup>, AAAS. Panels **d–f** adapted with permission from REF.<sup>71</sup>, ACS. Panels **g–i** adapted with permission from REF.<sup>72</sup>, © The Optical Society.

$$g(x) = \underbrace{\text{IFT}}_{\text{Block3}} \left[ \underbrace{H(k_x)}_{\text{Block2}} \cdot \underbrace{\text{FT}[f(x)]}_{\text{Block1}} \right] \quad (3)$$

Equation 3 governs the working of analogue computers based on the metasurface approach, which essentially consist of three distinct sub-blocks: a spatial Fourier transformer, FT, that takes the Fourier transform of the input field  $f(x)$  (as explained previously, the Fourier transformation can be performed using an optical lens); a properly designed metasurface with position-dependent transmission (or reflection) coefficient, corresponding to the transfer function of the operator of choice; and an inverse Fourier transformer, IFT, that takes the inverse Fourier transform of  $G(k_x) = F(k_x)H(k_x)$ , yielding the desired output field  $g(x)$ .

**Examples and applications.** An example of a metasurface computing system, designed to calculate the first-order derivative ( $\partial/\partial x$ ) of input signals, is shown in FIG. 3b. The system includes two graded-index dielectric lenses<sup>69</sup> that have a parabolic variation of permittivity  $\epsilon(x) = \epsilon_c(1 - (\pi x/2L)^2)$ , where  $L$  is the focal length of the lens. In the paraxial approximation, such an inhomogeneous material acts as a Fourier transformer<sup>69</sup>. The metasurface block is composed of a layered structure of two alternating materials, aluminium-doped zinc oxide (AZO) and silicon<sup>70</sup>, with different dissipation losses. The geometrical parameters of the metasurface are tailored such that it provides a position-independent transmission coefficient akin to the transfer function of the targeted operator,  $H(k_x) = ik_x$ . The simulated performance of the system is shown in FIG. 3c, and confirms that the transmitted field is, indeed, the derivative of the incident field distribution. Compared with the analogue differentiators based on 4F correlators, this system provides several advantages. In particular, by properly engineering the metasurface sub-block, the system can be adapted to perform more complex mathematical operations, such as local phase control, that are not achievable with standard spatial analogue filters. In addition, it provides higher-resolution reconstruction, because the metasurface sub-block can be deeply subwavelength. Alignment issues may also be reduced if the entire system can be manufactured in one block.

Several other computing systems based on the metasurface approach were proposed and experimentally demonstrated. For example, an analogue system based on a plasmonic meta-reflect array capable of performing a large variety of processing operations was demonstrated<sup>71</sup>. The unit cell of the metasurface, shown in FIG. 3d, is composed of silicon nanobricks arranged on top of a silica layer placed on an optically thick metallic film. By varying the size of the nanobricks ( $L_x$  and  $L_y$ ), the amplitude and phase of the reflected field can be independently controlled (FIG. 3e). This enables the realization of arbitrary transfer functions. Suppose, for example, that we want to realize the derivative  $\partial/\partial x$ . The associated transfer function ( $H(k_x) = ik_x$ ) implies a position-dependent reflection coefficient of the form  $|r| = R_0 x/L$ , in which  $-L < x < L$  is the length of the

metasurface array and  $R_0$  is a constant. The parameters of the metasurface can be tailored to achieve the desired reflection profile. The proper operation of the corresponding computing system was experimentally demonstrated by exciting the structure with a Gaussian derivative incident signal; the corresponding reflected field was the derivative of the incident field, confirming the proper functionality of the system (FIG. 3f).

Although this plasmonic metasurface can perform various mathematical operations, it suffers from some limitations: it has high absorption and low conversion efficiency, which stems from the use of lossy plasmonic materials. In addition, it is not compatible with complementary metal–oxide–semiconductor (CMOS) technology, hindering its integration within silicon photonic devices. These disadvantages were overcome by developing an all-dielectric metasurface computing system<sup>72</sup>. The metasurface was built from silicon nanoresonators placed on top of a silica spacer and a thick layer of silver (FIG. 3g). The amplitude and phase of the reflection coefficient of the metasurface as a function of the width ( $L_y$ ) and length ( $L_x$ ) of the silicon nanobricks are shown in FIG. 3h. The associated reflection coefficient spans the full phase range of 0 to  $2\pi$ , whereas the amplitude of the reflection can vary from 0 to 1 by varying  $L_y$  and  $L_x$ . Coupled to graded index lenses, these features enable the realization of arbitrary mathematical functionalities. As an example, a second-order differentiator was designed by properly structuring the nanobricks of the metasurface. When a sinc-shaped electric field,  $f(x) = \text{sinc}(x/6.8 \times 10^{-6})$ , was used as the input field, the reflected field was, indeed, its second-order derivative (FIG. 3i).

#### Acoustic computational metamaterials

In addition to their development in optics, computational metamaterials have been explored in another area of classical physics, namely, acoustics. Although acoustic computational metamaterials are not as fast as their optical counterparts, as they operate at the speed of sound, they could potentially be used to accelerate imaging and prospection methods by allowing more processing tasks to be performed analogically and in parallel. In addition, tremendous advances in surface acoustic-wave technology offer great potentialities for the miniaturization of acoustic analogue signal processors. For example, an acoustic computing system based on the metasurface approach<sup>73</sup> employed a metastructure with a unit cell composed of three tapered, labyrinthine, spiral components with varying radians,  $S_1$ ,  $S_2$  and  $S_3$  (FIG. 4a). By tuning  $S_1$ ,  $S_2$  and  $S_3$ , full control over both the amplitude (FIG. 4b) and the phase (FIG. 4c) of the transmitted field was achieved, providing the possibility of achieving a broad range of analogue computational tasks. As a specific example, a second-order linear differential equation solver was designed using such a metastructure. The transfer function of the targeted differential equation (FIG. 4d) was realized by precisely tuning the spiral radians of the unit cells. The functionality of the system was demonstrated in simulations by exciting the metasurface with a Gaussian incident field (FIG. 4e), which resulted in a transmitted pressure field (FIG. 4f) in perfect agreement

with the analytically predicted solution of the targeted ordinary differential equation (ODE).

This computing system is based on the metasurface approach. Green's function-based acoustic computation has also been implemented with metamaterials to perform specific-purpose computational tasks using acoustic signals. An acoustic spatial differentiator was, indeed, demonstrated based on the Green's function method<sup>74</sup>, and its structure is shown in FIG. 4g. It was built from a metamaterial composed of a square array of cross-shaped pipes. The holey structure of the metamaterial provides a reduced compressible volume for sound

propagation, effectively reducing the speed at which the acoustic wave travels<sup>75</sup>. As a result, the metamaterial acts like a high-index acoustic medium, confining sound and guiding it via total internal reflection (this is akin to the principle of dielectric slab waveguide in optics). At a specific incident angle, the characteristic impedance of the metamaterial matches that of the incident medium, air. This leads to a dip (zero) in the reflection spectrum, near which the Green's function of the structure can be approximated with a linearly varying function. At this condition, in real space, the structure serves as a first-order differentiator. The relevance of such kind

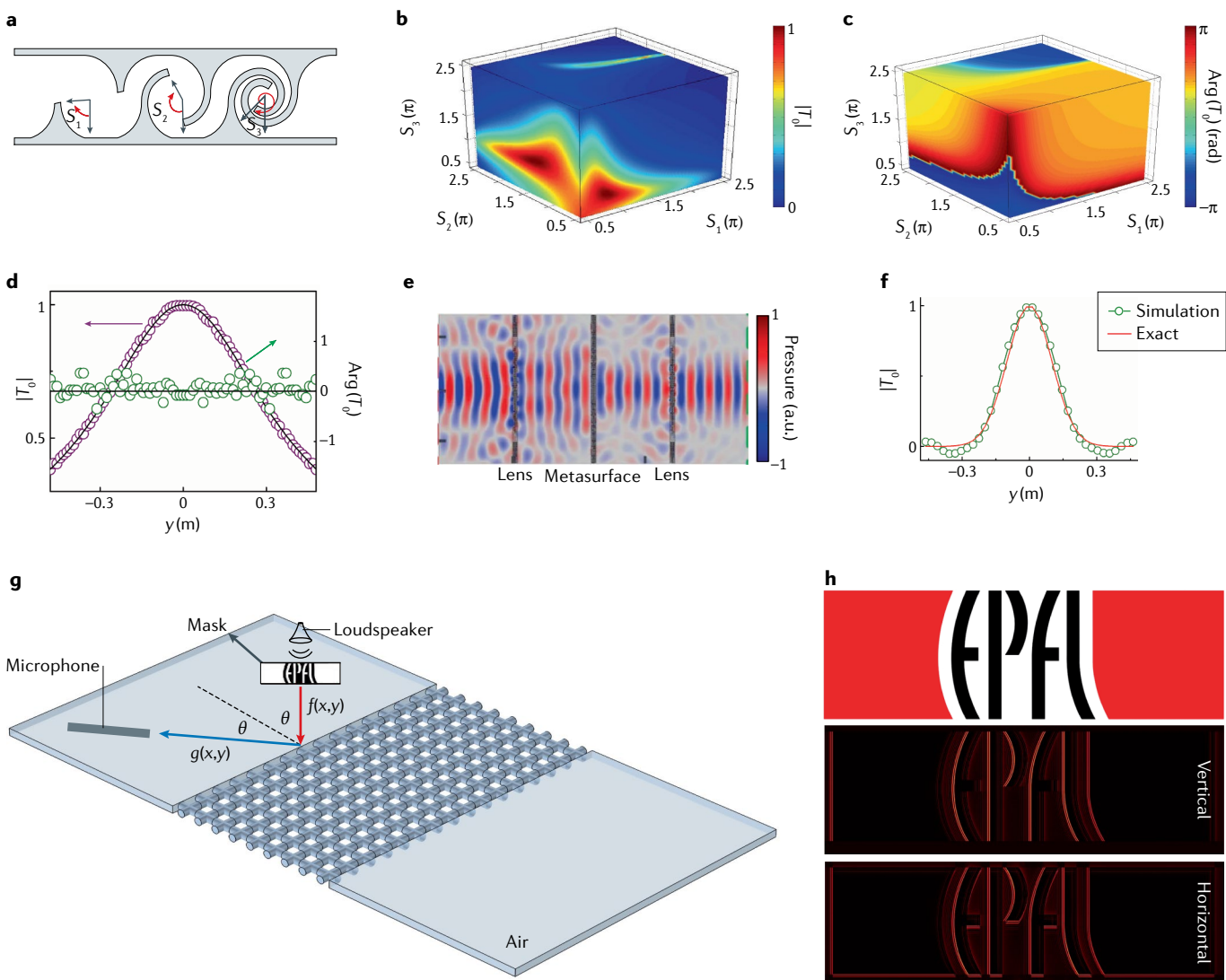


**Fig. 4 | Acoustic computational metasurfaces.** **a** | An acoustic metasurface computing system consisting of three tapered, labyrinthine components with varying spiral radians,  $S_1$ ,  $S_2$  and  $S_3$ . The complex path-coiling of the labyrinthine structures creates strong, multiple-scattering effects, leading to an extreme range of amplitudes and phases of the transmitted field. **b** | Amplitude of the transmission coefficient,  $T_0$ , as a function of  $S_1$ ,  $S_2$  and  $S_3$ . **c** | Phase of transmittance as a function of  $S_1$ ,  $S_2$  and  $S_3$ . **d** | Amplitude (purple) and phase (green) of the transmission spectrum associated with the transfer function of a second-order ordinary differential equation solver. **e** | The performance of the designed metasurface computing system is evaluated by simulating its response to the Gaussian

incident signal shown in this panel. **f** | The corresponding transmitted field, following the solution of the targeted ordinary differential equation. **g** | An acoustic computing system based on the Green's function approach. The structure consists of a half-wavelength high-index metamaterial, whose reflection coefficient drops to zero at some specific incident angle  $\theta$ . Near this zero, the reflection spectrum can be well estimated with the transfer function of the ideal differentiator. The incident field is modulated by a mask plane with a properly designed transparency pattern corresponding to the EPFL logo. **h** | Spatial vertical and horizontal edge detection based on the high-index acoustic computing metamaterial in panel **g**. Panels **a–f** adapted from REF.<sup>73</sup>, CC BY 4.0. Panels **g** and **h** adapted from REF.<sup>74</sup>, CC BY 3.0.

of a differentiator for acoustic-image edge detection is illustrated in FIG. 4h.

### Emerging directions

#### Wave-based equation solvers

**Solving linear differential equations.** Equations are ubiquitous in many areas of science, including mathematics, physics and engineering. Wave-based analogue computers such as those discussed in the previous sections represent an ideal platform for ultra-fast equation solving<sup>76,77</sup>. As a relevant example, we start by discussing first-order ODEs, with general form

$$\alpha f'(t) + \beta f(t) = g(t) \quad (4)$$

A wave-based analogue system returning the solution of Eq. 4 for given coefficients  $\alpha$  and  $\beta$  is schematically shown in FIG. 5a. Consider an arbitrary resonator with a Lorentzian spectral line shape around the resonance. The Green's function of the resonator is given by

$$H(\omega) = 1/(\alpha j(\omega - \omega_0) + \beta), \quad (5)$$

in which  $\alpha$  and  $\beta$  are arbitrary constants that depend on the quality factor of the resonator. The Green's function of Eq. 5 (plotted in FIG. 5b) is equivalent to the transfer function of the first-order ODE in Eq. 4, implying that, in the time domain, any Lorentzian resonator acts as a first-order ODE solver. In acoustics, such kind of functionality can be achieved by, for example, putting a defect inside a Bragg phononic crystal (FIG. 5c). In another example of an all-optical differential equation solver experimentally realized based on a resonance phenomenon<sup>74</sup>, the system was made of a silicon microring resonator coupled to two straight waveguides (FIG. 5d). Around the resonance frequency of the microring resonator, the transmission spectrum of this system exhibits a Lorentzian peak (FIG. 5e), corresponding to a first-order ODE with specific constant coefficients. Remarkably, the spectral characteristics of the structure can be tuned via a gate voltage applied to the microring resonator, enabling a wide control over the constant coefficients. To examine the performance of the differentiator, the microring resonator was excited with a Gaussian pulse. The corresponding transmitted signal was in excellent agreement with the solution of the targeted ODE (FIG. 5f).

Note that, in general, it is possible to solve higher-order ODEs by constructing a network of first-order ODE solvers with different transfer functions. As an example, let us suppose that we want to engineer a transfer function of order  $n$  ( $n$  may be arbitrarily high), corresponding to the following differential equation

$$f^n(t) + A_{n-1}f^{n-1}(t) + \dots + A_1f'(t) + A_0f(t) \\ = Bg(t). \quad (6)$$

The associated transfer function is given by

$$H(\omega) = \frac{B}{(j(\omega - \omega_0))^n + A_{n-1}(j(\omega - \omega_0))^{n-1} + \dots + A_1(j(\omega - \omega_0)) + A_0}. \quad (7)$$

By employing partial fractional decomposition,  $H(\omega)$  can be written as a summation of the form

$$H(\omega) = \sum_{i=1}^n \frac{K_i}{j(\omega - \omega_0) + \omega_0/2Q_i}, \quad (8)$$

where  $Q_i = -\omega_0/2P_i$ , in which  $P_i$  are the complex roots of the associated  $n$ th-order denominator polynomial, and  $K_i$  are complex constant coefficients. Equation 8 suggests that the transfer function of an arbitrary  $n$ th order ODE can be realized by adding the output signals of  $n$  different Lorentzian resonators with different quality factors  $Q_i$ . The summation can be performed in a fully analogue fashion using, for instance, standard directional couplers<sup>78</sup>.

**Solving integral equations.** Metamaterials have also been exploited to solve integral equations that cannot be directly solved using a Fourier transform. In particular, a metamaterial platform was proposed<sup>79</sup> to solve the general integral equation

$$g(u) = I_{\text{in}}(u) + \int_a^b K(u, v)g(v)dv, \quad (9)$$

in which  $I_{\text{in}}(u)$  is the input signal,  $g(v)$  is the unknown function and  $K(u, v)$  is the kernel associated with an arbitrary operator. Note that  $K(u, v)$  is assumed to have general dependence on  $u$  and  $v$ , not just on the difference  $u - v$ , which would correspond to a convolution, preventing, in general, the equation to be solved by using Fourier optics. The schematic of a metamaterial-based system solving Eq. 8 with the arbitrarily chosen kernel

$$K(u, v) = 0.06 \begin{cases} (4 - 4i)J_0(uv) \\ + 3 \exp\left[\frac{i2\pi}{5(u+v)} - (1 - 2i)\right] \end{cases} \quad (10)$$

is shown in FIG. 5g. In this system, the kernel  $K(u, v)$  is implemented using a binary metamaterial composed of air and polystyrene. The inhomogeneity of the metamaterial structure, described by an inhomogeneous relative permittivity  $\epsilon(x, y)$ , allows one to realize the desired kernel function  $K(u, v)$  using an optimization process.  $N$  feedback waveguides provide feedback to the system, adding the output of the metasurface  $\int_a^b K(u, v)g(v)dv$  to the input function  $I_{\text{in}}(u)$  at  $N$  different points across the  $[a, b]$  interval. In this discrete form, the system implements the equivalent  $N \times N$  matrix equation of Eq. 9. The prototype of the metamaterial structure, in which five metallic waveguides operating at the fundamental  $TE_{10}$  mode were used to sample the output across the desired range, is shown in FIG. 5h. The output signal measured at the first sampling waveguide, shown in FIG. 5i, is in excellent agreement with the theoretical solution of the targeted integral equation.

#### Topological and non-reciprocal computing

Wave-based analogue computers provide the possibility of carrying out specialized computational tasks with ultra-high speed, but they suffer from an important

limitation, which may hinder their applicability in large-scale applications. Unlike DSPs, in which disorder is not an issue thanks to the binarized or discretized nature of the input, wave-based analogue computers are typically fragile to noise and perturbations. In particular, the errors caused by geometrical imperfections can accumulate during series operation, degrading the performance of the analogue computer.

To tackle this issue, researchers have leveraged a particular class of metamaterials with non-trivial topology, known as topological metamaterial insulators. Such insulating artificial materials exhibit frequency band gaps in which no bulk wave propagation is possible. However, the particular topology of their band structure guarantees the presence of modes on their boundaries. Because the existence of these boundary modes

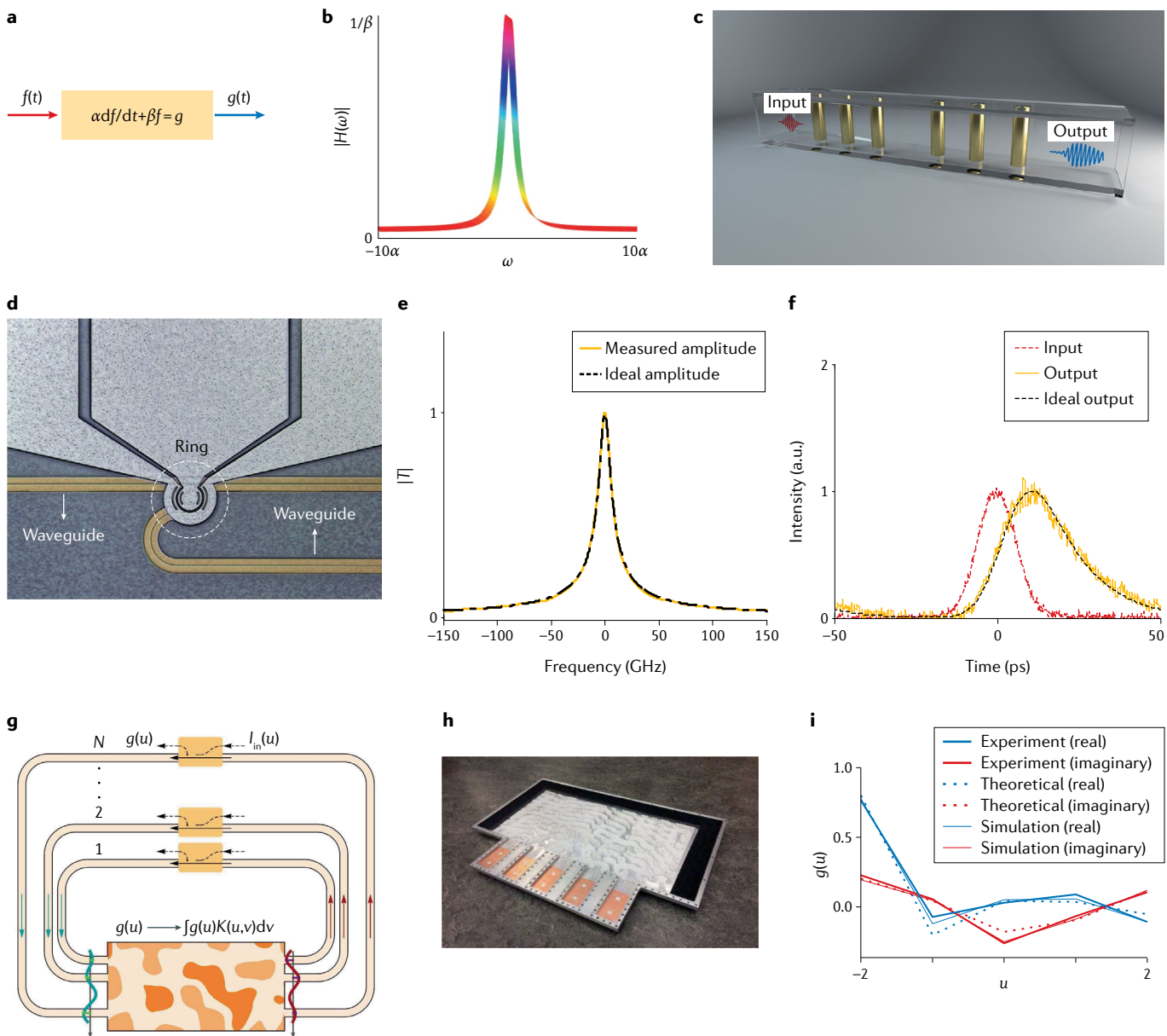


**Fig. 5 | Wave-based analogue equation solving.** **a** | A general equation solver, aimed at solving a first-order ordinary differential equation (ODE). **b** | Green's function of a Lorentzian resonator, matching the transfer function of the first-order differential equation. **c** | A first-order ODE solver based on resonance tunnelling through a Bragg band gap. **d** | An optical first-order ODE solver based on the resonance of a microring resonator fabricated on a silicon wafer. **e** | Amplitude (yellow) of the transfer function of the microring resonator around its resonance frequency, which is equivalent to that of a first-order ODE with specific constant coefficients (black). **f** | Experimental demonstration of first-order ODE solving based on the microring resonator in panel **d**.

The measured output field matches the solution of the target ODE. **g** | A metasurface platform solving integral equations of general form  

$$g(u) = I_{in}(u) + \int_a^b K(u, v)g(v)dv$$

where  $I_{in}(u)$  is the input signal,  $g(v)$  is the unknown function and  $K(u, v)$  is the kernel associated with an arbitrary operator. The equation solver consists of a metasurface realizing the kernel of the integral equation and  $N$  feedback waveguides adding the output of the metasurface to the input signal at specific sampling points. **h** | A photograph of the metasurface structure realizing the proposal in panel **g**. **i** | Demonstration of the proper performance of the integral equation solver. Panel **c** adapted from REF.<sup>86</sup>, CC BY 4.0. Panels **d-f** adapted from REF.<sup>134</sup>, CC BY 4.0. Panels **g-i** adapted with permission from REF.<sup>79</sup>, AAAS.

is a direct consequence of the topology of the bulk band structure of the system, it cannot be influenced by continuous deformation, such as that induced by the local introduction of small defects or geometrical imperfections. Instead, the topology can only change through a global, drastic modification of the system that would entirely destroy its insulating property. As a result, the edge modes of topological structures exhibit strong immunity to small and moderate levels of imperfections<sup>80–85</sup>, provided that the disorder does not break a symmetry on which the topological order depends. Motivated by these advances, a new class of wave-based analogue signal processors leveraging these robust topological boundary modes was recently introduced. Such topological analogue signal processors<sup>86</sup>, for example, implement the Green's function method using resonance tunnelling through the boundary mode of a 1D topological wave insulator, thereby, featuring strong robustness against a large range of defect types.

To provide a specific example, consider the configuration shown in FIG. 6a (left), consisting of an acoustic pipe, inside which a sonic crystal built from solid cylindrical rods is arranged. The two halves of the phononic crystal include two insulating lattices with different topological properties, inspired by a specific topological arrangement known as the Su–Schrieffer–Heeger (SSH) scheme, initially discovered in condensed-matter systems<sup>87</sup>. The difference between the topological invariants of the two insulating halves of the system leads to an interface mode located at its centre, which is symmetry-protected, as long as all the rods have the same diameter. This edge mode has a Lorentzian spectral line shape, which, as explained in the previous section, can be utilized for solving first-order ODEs. Remarkably, the frequency of the edge mode is pinned by topology, even if some relatively large disorder is imparted to the positions of the rods. Indeed, after randomly shifting the rods (FIG. 6a, right), the transfer function of the equation solver, and, as a result, the corresponding output signal, are not affected. The boundary mode is pinned to a certain frequency, as long as the position disorder is not strong enough to turn it into an insulator, and as long as the symmetry protection (identical rod diameters) is present<sup>86</sup>.

This system has been used to perform analogue signal processing (FIG. 6b). The measured transfer function of the structure, sketched in the middle panel of the figure, exhibits a peak at the resonance frequency of the topological edge mode ( $f_0$ ). To characterize the performance of the system, the waveguide was excited with an arbitrarily shaped signal (left panel), modulated at  $f_0$ . The corresponding measured output signal, shown on the right side of the panel, follows the solution of the targeted first-order ODE (dashed line). The functionality of the equation solver is immune to position disorder, as shown in the lower part of FIG. 6b. Note that, as we explained in the previous section, by constructing a network of first-order ODE solvers using directional couplers, one can achieve transfer functions corresponding to higher-order ODEs. FIGURE 6c, for instance, demonstrates the possibility of solving a second-order

ODE by subtracting the output signals of two topological first-order systems with tailored dissipation losses.

Another way to achieve robust computing is to use the one-way modes propagating in non-reciprocal optical structures. Such non-reciprocal effects can be obtained by breaking time-reversal symmetry using, for example, a magneto-optic material under an external magnetic field<sup>88,89</sup>. For instance, the one-way character of magnetized SPPs was used to realize a spatial differentiator immune to backscattering<sup>90</sup>. The non-reciprocal differentiator consisted of an opaque medium film ( $\epsilon = -1$ ) coated on a magnetic substrate (InSb, FIG. 6d). A static magnetic field was applied to the substrate, breaking time-reversal symmetry and leading to one-way SPP excitation. The reflection coefficient of the structure has a dip near the resonance frequency of the SPP mode, which can be employed to perform spatial differentiation, as we discussed previously. The mode profile of the structure when it is excited with a Gaussian incident field at the frequency (and the momentum) of the SPP mode is shown in FIG. 6e. As expected, the reflected field has a Gaussian derivative profile. Remarkably, there is no backscattering, even in the presence of geometrical irregularities at the interface between the two layers of the structure.

### Metamaterials for machine learning

As mentioned above, one important advantage of analogue approaches to perform computations is the ability to process information in parallel, without restrictions on the operating speed. This advantage becomes important when a large amount of data has to be processed, for instance, when performing large matrix multiplications or decoding the information hidden in a large amount of measurements. Such decoding tasks can be highly non-trivial, especially if no analytical description or physical modelling of the relation between the information and the data is available (for example, imaging or recognizing objects using waves through an unknown multiple-scattering environment). One way to tackle such problems is to use machine learning<sup>91</sup>, a modern processing technique in which a computer is given the opportunity to learn on some training data, for which the encoded information is known, before being capable of processing unknown data. Machine learning often requires some particular form of non-linearity, making it much more complicated than the linear analogue functionalities described so far, because non-linear operations cannot be tackled by Fourier optics approaches. The training process, during which the system learns the intricate links between the encoded information and the data, and reconfigures itself to be able to process new data, is often based on a neural network<sup>92</sup>, an interconnected, reconfigurable network of artificial neurons connecting the data and the information to be retrieved.

The neurons and their connections, called edges, are generally assembled into a layered architecture, in which the output of each neuron is a weighted, non-linear function of its inputs. The reconfigurable part of the network is represented by weights that increase or decrease the signal at a connection, a process somehow inspired by biological neural networks that constitute animal brains.

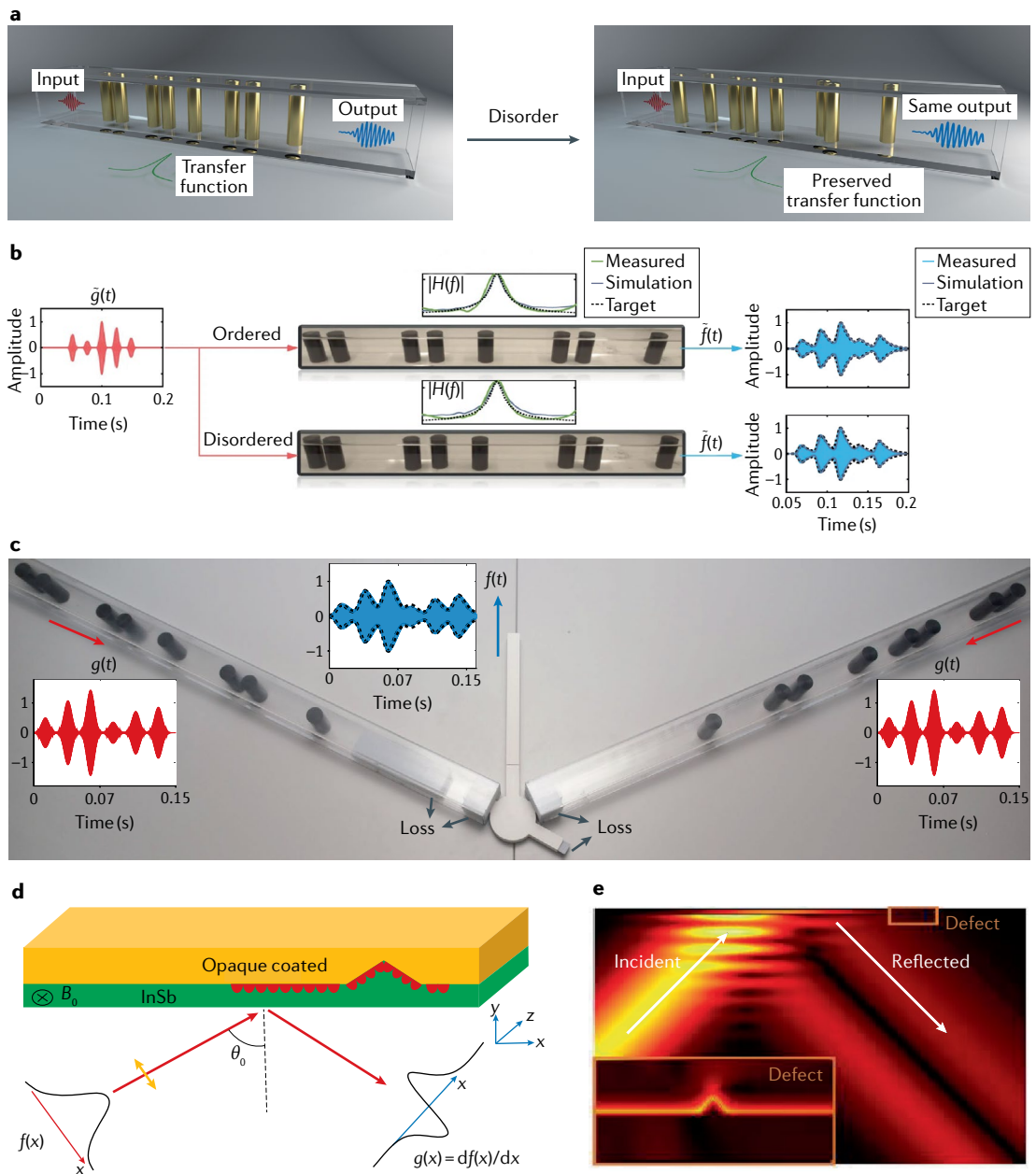


**Fig. 6 | Robust analogue signal processing.** **a** A topological analogue signal processor solving first-order differential equations (left). The equation solver is based on the edge mode of a 1D Su-Schrieffer-Heeger (SSH)-like array of nylon plastic rods arranged inside an acoustic waveguide. Right: some disorder is added to the system by randomly changing the positions of the obstacles. The topological equation solver is robust to the disorder. **b** Experimental demonstration of topological analogue signal processing using the system in panel a. The transfer function of the system (middle panel) exhibits a peak near the resonance frequency of the edge mode, following the transfer function of a first-order ordinary differential equation (ODE). The corresponding output signal is, therefore, identical to the solution of the ODE (dashed line). The system preserves its functionality even in the presence of disorder (bottom signal path). **c** Realization of a second-order ODE solver by subtracting the output signals of two different first-order ODE solvers (like the ones in panels a and b) from each other. The subtraction is performed using an acoustic rat-race coupler. **d** Spatial differentiation based on non-reciprocal, one-way magnetized surface plasmon polaritons formed at the interface between an opaque medium film and the InSb substrate. **e** Demonstration of the proper functioning of the differentiator and its robustness to disorder. Panels a-c adapted from REF.<sup>86</sup>, CC BY 4.0. Panels d and e adapted with permission from REF.<sup>90</sup>, APS.

Neural networks are traditionally implemented in the digital domain and work on digital data. However, when practical data originate from a measurement operation with a large amount of analogue sensors, it may be useful to perform, as much as possible, the parallel processing

of the information in the analogue domain, which can yield considerably higher speed of operation and processing efficiency, and lower power consumption.

In this section, we describe two categories of efforts in which metamaterials are combined with machine

learning for this purpose. This field is very broad and active, hence, we specifically focus on works in which metamaterials have a computational role, rather than on research that leverages machine learning as a design tool for metamaterials. Let us start with an elementary information-theoretic description of a sensing process, represented in FIG. 7a. Part of the information that we are interested in, encoded in a field that propagates in a potentially complex medium, is first sampled via some physical mechanism, typically involving sensors. This measurement process may lead to a dataset in which the information of interest is present in part or in full. Sometimes, more information than needed is contained in the data. Nevertheless, the second step is generally

to decode these data using machine learning to extract the desired information. This second step involves a series of large, linear matrix multiplications, application of non-linear functions and successive adjustments of weights. The green labels in FIG. 7a highlight at which steps of this process metamaterials can be used to perform a computational task.

A first category of computing metamaterials is concerned with the encoding part. The information carried by a wave field is either contained in the spatial degrees of freedom of the wave or in its frequency degrees of freedom. Metamaterials, composed of resonant scatterers with large scattering cross section, can possess both spatial dispersion (linked to multiple scattering)

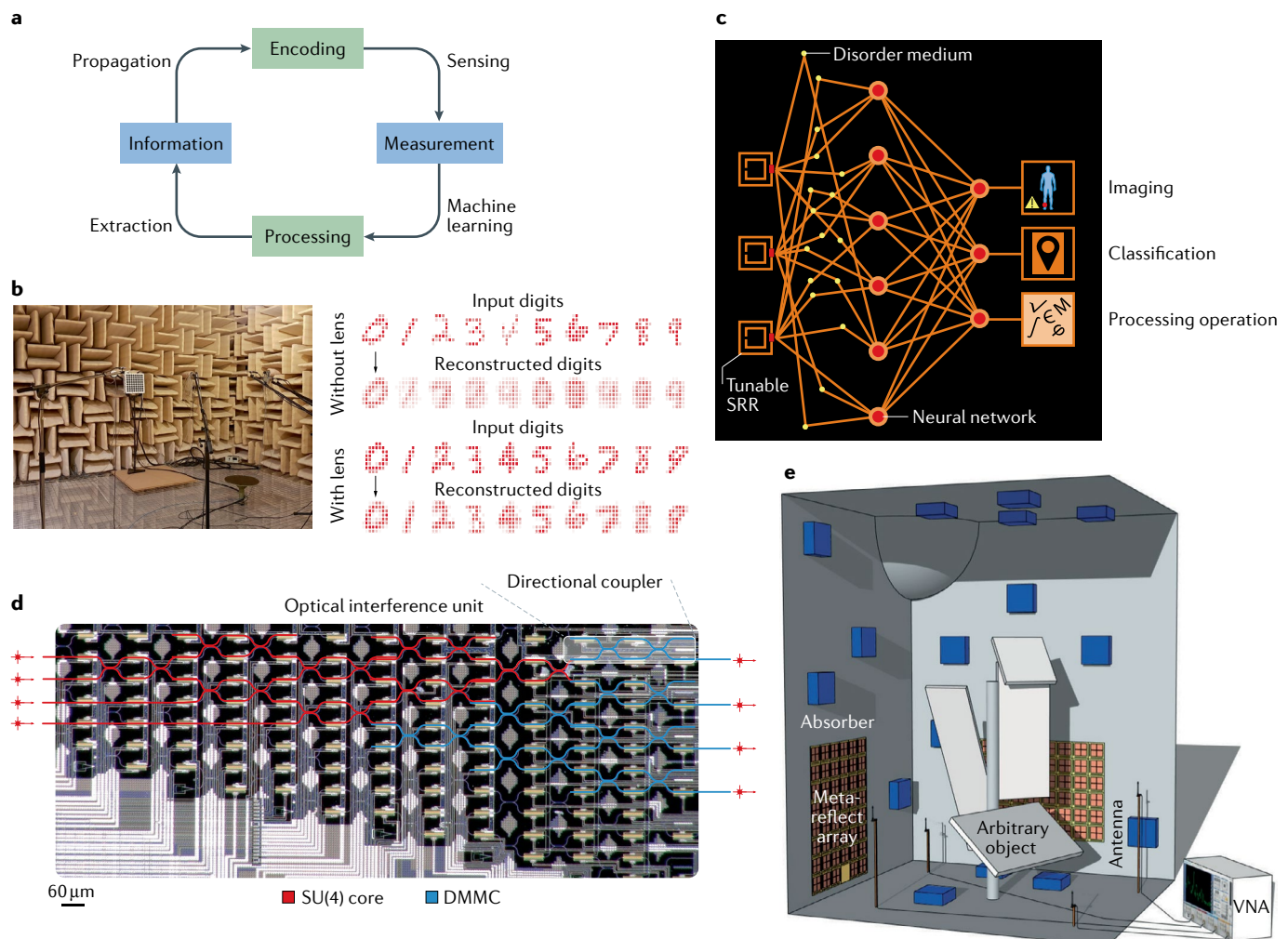


**Fig. 7 | Machine learning with metamaterials.** **a** | A typical sensing process, where information carried by a wave field is encoded in measured data. These data are processed by a machine-learning method to extract the desired information. **b** | Example of a metamaterial used to help the learning process by acting at the encoding stage. A subwavelength acoustic source is generated by a loudspeaker array and shaped as a handwritten digit. The acoustic far field is sampled at four different points using microphones. After learning, a neural network is not able to reconstruct or classify the digits, because the information about subwavelength features of the source ( $\lambda/30$ ) cannot reach the far field. By placing a locally resonant metamaterial in the near field (not shown in the picture), this information can be encoded in the far field, enabling the reconstruction and classification of the digits

by the neural network<sup>110</sup>. **c** | Concept of learned sensing, where the first layer of the neural network is a physically reconfigurable layer that is optimized during the learning process to focus only on measuring the relevant information<sup>104</sup>. **d** | Microscope image of a silicon photonic neural network used to implement linear matrix multiplication for deep learning. **e** | A chaotic microwave cavity with reconfigurable boundary conditions implemented using programmable metasurfaces can be used to perform very efficient and fast large-matrix multiplication. DMMC, diagonal matrix multiplication core; SRR, split-ring resonator; VNA, vector network analyser. Panel **b** reprinted from REF.<sup>93</sup>, CC BY 4.0. Panel **c** image courtesy of Philipp del Hougne, Université Côte d'Azur, France. Panel **d** adapted from REF.<sup>106</sup>, Springer Nature Limited. Panel **e** reprinted from REF.<sup>107</sup>, CC BY 4.0.

and frequency dispersion (linked to inertial response). Therefore, they can process both the spatial and the temporal information carried by the wave field, for instance, to make sure that a maximum amount of the desired information is present in the measured data. A practical example is shown in FIG. 7b. An array of loudspeakers (placed in an anechoic chamber) creates an acoustic source with spatial features much smaller than the acoustic wavelength,  $\lambda$ , at the frequency of operation (the details are smaller than  $\lambda/30$ ), drawing some handwritten digits taken out of the Modified National Institute of Standards and Technology (MNIST) database. Four microphones are used to measure the acoustic pressure at four points in the far field. By training a neural network on these data, it is not possible to image the digits, because the information about subwavelength features is evanescent and does not reach the far field. However, by using a metamaterial built from an ensemble of Helmholtz resonators placed in the near field, the information contained in the evanescent fields can be encoded into information carried to the measurement points by propagating waves. In the presence of such a locally resonant metamaterial, the neural network can image and classify the digits<sup>93</sup>.

A second category of machine-learning systems in which metamaterials or metasurfaces have a computing role is based on an approach called learned sensing<sup>94–96</sup>. In such systems, one stops looking at the encoding and processing tasks separately, which typically leads to the acquisition of information that is irrelevant for the target task. Instead, one optimizes the entire sensing cycle at once by making sure that the system only acquires and processes the part of the information that is needed, sensing and learning at the same time. This idea emerged in the context of computational imaging using metamaterials, in which, originally, the metamaterials did not have any computing role related to machine learning but were used at the encoding level to implement compressive-sensing strategies<sup>97–100</sup>, exploiting either frequency selection or reconfigurability. In compressive-sensing strategies, a scene is illuminated with random or orthogonal patterns, which multiplexes all information. However, a lot of this information may be irrelevant. A first step along the route from compressive to learned sensing was taken by incorporating metasurfaces into sensing processes leveraging artificial-intelligence methods<sup>101–103</sup>. The concept of learned sensing then naturally emerged, inspired by developments in the optical-imaging communities<sup>95</sup>. The idea, represented in FIG. 7c, is to interpret a reconfigurable acquisition layer (for example, a few reconfigurable SRRs coupled to an ensemble of non-reconfigurable resonant dipoles, represented by the yellow dots in the figure) as an additional trainable layer of the machine-learning system (the rest of it may remain digital). Therefore, the jointly learned measurement and processing settings will select only the relevant information when measuring novel data. This idea, which effectively makes the computation much more efficient<sup>104</sup>, was recently experimentally validated<sup>105</sup>.

Finally, we stress that even some of the remaining digital part of the sensing process can be implemented

analogically with waves. Indeed, a metamaterial or an artificial structure can be involved at a later step, namely, in the heavy linear matrix multiplications involved in the processing, in order to gain efficiency in terms of speed or power consumption. This is motivated by the ability of passive-wave-based systems to perform many operations in parallel, as an alternative to digital systems subject to the fundamental thermal limits of Moore's law. For instance, a neural network based on silicon nanophotonic circuits has been proposed and applied to perform deep learning<sup>106</sup>. In this system, a reconfigurable mesh of waveguides (FIG. 7d) was used to implement linear matrix multiplication, whereas the non-linearity was added digitally. Another interesting approach to achieve reconfigurable matrix multiplication at microwave frequencies is the use of chaotic cavities, such as a standard indoor environment at a Wi-Fi frequency. By making the cavity reconfigurable by placing programmable metasurfaces on the room walls<sup>107</sup> (FIG. 7e), a wide variety of very large matrix multiplications can be performed. Rather than engineering a material with intricate design, this approach takes a random material and tweaks it with a programmable metamaterial to implement the desired functionality, thereby, removing the prohibitive sensitivity to fabrication inaccuracies. At optical frequencies, spatial light modulators may be used to build reconfigurable metasurfaces and achieve similar multiplication tasks at higher frequencies and lower scales<sup>108,109</sup>.

## Conclusion and perspectives

In this Review, we have discussed the recent progress in the field of computational metamaterials and outlined several examples of its practical applications in modern engineering, including equation solving, image processing and machine learning. We close by identifying a longer-term outlook on this emerging field and discuss the key challenges that should be addressed in future work.

An interesting idea, proposed in a few recent papers<sup>110–112</sup>, is multifunctional wave-based analogue computing, in which several computational tasks are performed simultaneously on different input channels. Such kind of operation provides the unique possibility of parallel processing of information, substantially enhancing the speed of computation. For optical signals, multifunctional analogue computing can be achieved by, for example, a metasurface composed of anisotropic components. The anisotropic behaviour of such a structure allows one to manipulate the reflection and transmission of the transverse-electric and TM polarization degrees of freedom independently. This enables performing multiple signal-processing tasks at once. Extensions of parallel computing to an arbitrary number of channels may leverage media with many spatial or temporal degrees of freedom, such as disordered multiple-scattering systems<sup>113</sup>. Not only does the parallel operation of such kinds of computing structures enable enhancing the speed of processing but it also provides the possibility of saving a lot of power, avoiding the use of large-scale electronic systems and the associated challenging thermal-dissipation problems, which are currently limiting the continuation of Moore's law.

Most of the computational metamaterials discussed in this Review are related to linear functionalities. With the development of learning-based approaches, investigating the possibility of performing non-linear analogue processing operations with computational metamaterials is a clear opportunity for future research. We highlighted the relevance of wave-based analogue computers for machine learning (which inherently requires non-linear processing), but research on reconfigurable or non-linear metamaterials as a way to perform part or all of a sensing process is still in its infancy. In addition, non-linear computational metamaterials can be used for other purposes, such as complex non-linear equation solving, or to implement analogically many of the non-linear, filtering, image-processing methods employed in digital technologies. Non-linear interaction in such kinds of computational metamaterials, combined with reconfigurability, also represents an opportunity for the realization of programmable analogue computing systems, behaving as the analogue, wave-based counterpart of electronic field-programmable gate arrays.

Investigating the effect of undesired disorder on computational metamaterials is another important subject for future research. As we discussed in this Review, topological computational structures are robust against disorder such as impurities and defects. Yet, their much-sought robustness is ultimately restricted, when the imperfections are large, by Anderson localization<sup>114</sup>, which leads to a progressive filling of the band gap of the structure with localized bulk states in the regime of strong randomness. Although this effect seems to be harmful at first glance, the fact that introducing disorder to a system can induce a topological phase transition is very encouraging: it suggests that the opposite transition, from a trivial structure to a topological disordered one, is also possible<sup>115</sup>. Such a transition suggests the fascinating possibility of performing specific, well-defined computational tasks in the regime of dominant randomness, as suggested in a recent article<sup>116</sup>. These findings suggest that combining topologically robust computing metamaterials and disorder-based computations may be a promising direction for future research.

Most computational metamaterials, including the ones reviewed here, are resonance based, imposing certain restrictions on their performance, notably in terms of the operational bandwidth. Broadening the bandwidth of computational metamaterials is important for some applications. Some steps along this direction have already been taken with wave-based computing systems designed based on wavelength-independent phenomena such as the Brewster effect<sup>10</sup> or relatively broadband effects like the spin Hall effect<sup>45,117,118</sup>. Yet, active wave systems may represent an unexplored way to achieve wideband analogue computation: because they are not subject to restrictive sum-rule bandwidth constraints as passive systems, they can push the limits on bandwidth up to what is allowed by causality and stability. The field of active metamaterials<sup>119–123</sup> may be mature enough to offer a unique solution to maintain absorption losses to acceptable levels, enhance the signal-to-noise ratio and the bandwidth, or provide reconfigurability<sup>123</sup>.

Machine learning systems based on computing metamaterials have only been proposed in hybrid analogue-to-digital sensing systems, but research on fully analogue machine-learning systems is another interesting route, placed at the boundary between wave engineering and artificial intelligence<sup>124–130</sup>. For this, a source of non-linearity may be introduced in the physical layers to enable learning, exploiting Kerr dielectrics or optomechanical resonators in photonics, or controlled geometrical or electromechanical non-linearities in acoustics<sup>131</sup>. Analogue Ising machines<sup>132,133</sup> may also be developed to solve specific, non-deterministic, polynomial-time hard (NP-hard) problems. On the far horizon, one may dream of combining wave-engineering techniques with machine learning to enable the realization of a new generation of ‘auto-computers’ functioning without any specific manual operation and programming. Such intelligent computational systems may enable the solution of a wide variety of physical, mathematical and engineering problems that are too complex in reasoning or cannot be described using simple mathematical language. This suggests a very bright future for computational metamaterials.

Published online 19 October 2020

1. Lim, J. S. et al. *Digital Signal Processing* (Massachusetts Institute of Technology, 1987).
2. Solli, D. R. & Jalali, B. Analog optical computing. *Nat. Photon.* **9**, 704–706 (2015).
3. Small, J. S. General-purpose electronic analog computing: 1945–1965. *IEEE Ann. Hist. Comput.* **15**, 8–18 (1993).
4. Silva, A. et al. Performing mathematical operations with metamaterials. *Science* **343**, 160–163 (2014).
5. Engheta, N. & Ziolkowski, R. W. (eds) *Metamaterials: Physics and Engineering Explorations* (Wiley, 2006).
6. Pendry, J. B. Negative refraction makes a perfect lens. *Phys. Rev. Lett.* **85**, 3966 (2000).
7. Gansel, J. K. et al. Gold helix photonic metamaterial as broadband circular polarizer. *Science* **325**, 1513–1515 (2009).
8. Zhang, W., Cheng, K., Wu, C., Li, H. Y. & Zhang, X. Implementing quantum search algorithm with metamaterials. *Adv. Mater.* **30**, 1703986 (2018).
9. Li, L. & Cui, T. J. Information metamaterials—from effective media to real-time information processing systems. *Nanophotonics* **8**, 703–724 (2019).
10. Xie, Y. et al. Acoustic holographic rendering with two-dimensional metamaterial-based passive phased array. *Sci. Rep.* **6**, 35437 (2016).
11. Zhou, J. et al. Optical edge detection based on high-efficiency dielectric metasurface. *Proc. Natl. Acad. Sci. USA* **116**, 11137–11140 (2019).
12. Molerón, M. & Daraio, C. Acoustic metamaterial for subwavelength edge detection. *Nat. Commun.* **6**, 8037 (2015).
13. Memoli, G. et al. Metamaterial bricks and quantization of meta-surfaces. *Nat. Commun.* **8**, 14608 (2017).
14. Khorasaninejad, M. et al. Metalenses at visible wavelengths: Diffraction-limited focusing and subwavelength resolution imaging. *Science* **352**, 1190–1194 (2016).
15. High, A. A. et al. Visible-frequency hyperbolic metasurface. *Nature* **522**, 192–196 (2015).
16. Tran, M. C. et al. Broadband microwave coding metamaterial absorbers. *Sci. Rep.* **10**, 1810 (2020).
17. Fan, W., Yan, B., Wang, Z. & Wu, L. Three-dimensional all-dielectric metamaterial solid immersion lens for subwavelength imaging at visible frequencies. *Sci. Adv.* **2**, e1600901 (2016).
18. Cui, T. J., Qi, M. Q., Wan, X., Zhao, J. & Cheng, Q. Coding metamaterials, digital metamaterials and programmable metamaterials. *Light Sci. Appl.* **3**, e218 (2014).
19. Goodman, J. W. *Introduction to Fourier Optics* (Roberts, 2005).
20. Athale, R. & Psaltis, D. Optical computing: past and future. *Opt. Photonics News* **27**, 32–39 (2016).
21. Kou, S. S. et al. On-chip photonic Fourier transform with surface plasmon polaritons. *Light Sci. Appl.* **5**, e16034 (2016).
22. Zhou, Y., Zheng, H., Kravchenko, I. I. & Valentine, J. Flat optics for image differentiation. *Nat. Photonics* **14**, 316–323 (2020).
23. Bykov, D. A., Doskolovich, L. L., Bezus, E. A. & Soifer, V. A. Optical computation of the Laplace operator using phase-shifted Bragg grating. *Opt. Express* **22**, 25084–25092 (2014).
24. Liu, X. & Shu, X. Design of an all-optical fractional-order differentiator with terahertz bandwidth based on a fiber Bragg grating in transmission. *Appl. Opt.* **56**, 6714–6719 (2017).
25. Wesemann, L. et al. Selective near-perfect absorbing mirror as a spatial frequency filter for optical image processing. *APL Photonics* **4**, 100801 (2019).

26. Karimi, P., Khavasi, A. & Khaleghi, S. S. M. Fundamental limit for gain and resolution in analog optical edge detection. *Opt. Express* **28**, 898–911 (2020).
27. Zangeneh-Nejad, F., Khavasi, A. & Rejaei, B. Analog optical computing by half-wavelength slabs. *Opt. Commun.* **407**, 338–343 (2018).
28. Zhang, J., Ying, Q. & Ruan, Z. Time response of plasmonic spatial differentiators. *Opt. Lett.* **44**, 4511–4514 (2019).
29. Hwang, Y., Davis, T. J., Lin, J. & Yuan, X. C. Plasmonic circuit for second-order spatial differentiation at the subwavelength scale. *Opt. Express* **26**, 7368–7375 (2018).
30. Dong, Z., Si, J., Yu, X. & Deng, X. Optical spatial differentiator based on subwavelength high-contrast gratings. *Appl. Phys. Lett.* **112**, 181102 (2018).
31. Bezus, E. A., Doskolovich, L. L., Bykov, D. A. & Soifer, V. A. Spatial integration and differentiation of optical beams in a slab waveguide by a dielectric ridge supporting high-Q resonances. *Opt. Express* **26**, 25156–25165 (2018).
32. Lv, Z., Ding, Y. & Pei, Y. Acoustic computational metamaterials for dispersion Fourier transform in time domain. *J. Appl. Phys.* **127**, 123101 (2020).
33. Eftekhari, F., Gómez, D. E. & Davis, T. J. Measuring subwavelength phase differences with a plasmonic circuit — an example of nanoscale optical signal processing. *Opt. Lett.* **39**, 2994–2997 (2014).
34. Guo, C., Xiao, M., Minkov, M., Shi, Y. & Fan, S. Isotropic wavevector domain image filters by a photonic crystal slab device. *JOSA A* **35**, 1685–1691 (2018).
35. Guo, C., Xiao, M., Minkov, M., Shi, Y. & Fan, S. Photonic crystal slab Laplace operator for image differentiation. *Optica* **5**, 251–256 (2018).
36. Davis, T. J., Eftekhari, F., Gómez, D. E. & Roberts, A. Metasurfaces with asymmetric optical transfer functions for optical signal processing. *Phys. Rev. Lett.* **123**, 013901 (2019).
37. Wu, W., Jiang, W., Yang, J., Gong, S. & Ma, Y. Multilayered analog optical differentiating device: performance analysis on structural parameters. *Opt. Lett.* **42**, 5270–5273 (2017).
38. Fang, Y., Lou, Y. & Ruan, Y. On-grating graphene surface plasmons enabling spatial differentiation in the terahertz region. *Opt. Lett.* **42**, 3840–3843 (2017).
39. Idemen, M. M. *Discontinuities in the Electromagnetic Field* Vol. 40 (Wiley, 2011).
40. Youssefi, A., Zangeneh-Nejad, F., Abdollahramezani, S. & Khavasi, A. Analog computing by Brewster effect. *Opt. Lett.* **41**, 3467–3470 (2016).
41. Chen, Z. et al. Graphene controlled Brewster angle device for ultra broadband terahertz modulation. *Nat. Commun.* **9**, 4909 (2018).
42. Zangeneh-Nejad, F. & Khavasi, A. Spatial integration by a dielectric slab and its planar graphene-based counterpart. *Opt. Lett.* **42**, 1954–1957 (2017).
43. Zhu, T. et al. Plasmonic computing of spatial differentiation. *Nat. Commun.* **8**, 15391 (2017).
44. Ma, C., Kim, S. & Fang, N. X. Far-field acoustic subwavelength imaging and edge detection based on spatial filtering and wave vector conversion. *Nat. Commun.* **10**, 204 (2019).
45. Zhu, T. et al. Generalized spatial differentiation from the spin Hall effect of light and its application in image processing of edge detection. *Phys. Rev. Appl.* **11**, 034043 (2019).
46. Kwon, H., Sounas, D., Cordaro, A., Polman, A. & Alù, A. Nonlocal metasurfaces for optical signal processing. *Phys. Rev. Lett.* **121**, 173004 (2018).
47. Cordaro, A., Kwon, H., Sounas, D., Koenderink, A. F., Alù, A. & Polman, A. High-index dielectric metasurfaces performing mathematical operations. *Nano Lett.* **19**, 8418–8423 (2019).
48. Kwon, H., Cordaro, A., Sounas, D., Polman, A. & Alù, A. Dual-polarization analog 2D image processing with nonlocal metasurfaces. *ACS Photonics* **7**, 1799–1805 (2020).
49. Zhou, Y. et al. Analog optical spatial differentiators based on dielectric metasurfaces. *Adv. Opt. Mater.* **8**, 1901523 (2020).
50. Chen, H., An, D., Li, Z. & Zhao, X. Performing differential operation with a silver dendritic metasurface at visible wavelengths. *Opt. Express* **25**, 26417–26426 (2017).
51. Roberts, A., Gómez, D. E. & Davis, T. J. Optical image processing with metasurface dark modes. *JOSA A* **35**, 1575–1584 (2018).
52. Wang, L., Li, L., Li, Y., Zhang, H. C. & Cui, T. J. Single-shot and single-sensor high super-resolution microwave imaging based on metasurface. *Sci. Rep.* **6**, 26959 (2016).
53. Minovich, A. E. et al. Functional and nonlinear optical metasurfaces. *Laser Photonics Rev.* **9**, 195–213 (2015).
54. Gao, L. H. et al. Broadband diffusion of terahertz waves by multi-bit coding metasurfaces. *Light Sci. Appl.* **4**, e324 (2015).
55. Huo, P. et al. Photonic spin-multiplexing metasurface for switchable spiral phase contrast imaging. *Nano Lett.* **4**, 2791–2798 (2020).
56. Wang, H. et al. Off-axis holography with uniform illumination via 3D printed diffractive optical elements. *Adv. Opt. Mater.* **7**, 1900068 (2019).
57. Zuo, S. Y., Wei, Q., Cheng, Y. & Liu, X. J. Mathematical operations for acoustic signals based on layered labyrinthine metasurfaces. *Appl. Phys. Lett.* **110**, 011904 (2017).
58. Kamali, S. M. et al. Angle-multiplexed metasurfaces: encoding independent wavefronts in a single metasurface under different illumination angles. *Phys. Rev. X* **7**, 041056 (2017).
59. Liu, Z., Zhu, D., Rodrigues, S. P., Lee, K. T. & Cai, W. Generative model for the inverse design of metasurfaces. *Nano Lett.* **18**, 6570–6576 (2018).
60. Pfeiffer, C. & Grbic, A. Biaxialisotropic metasurfaces for optimal polarization control: Analysis and synthesis. *Phys. Rev. Appl.* **2**, 044011 (2014).
61. Bao, L. et al. Design of digital coding metasurfaces with independent controls of phase and amplitude responses. *Appl. Phys. Lett.* **113**, 063502 (2018).
62. Liu, T., Chen, F., Liang, S., Gao, H. & Zhu, J. Subwavelength sound focusing and imaging via gradient metasurface-enabled spoof surface acoustic wave modulation. *Phys. Rev. Appl.* **11**, 034061 (2019).
63. Sun, S., He, Q., Hao, J., Xiao, S. & Zhou, L. Electromagnetic metasurfaces: physics and applications. *Adv. Opt. Photonics* **11**, 380–479 (2019).
64. Zhang, L., Mei, S., Huang, K. & Qiu, C. W. Advances in full control of electromagnetic waves with metasurfaces. *Adv. Opt. Mater.* **4**, 818–833 (2016).
65. He, Q., Sun, S., Xiao, S. & Zhou, L. High-efficiency metasurfaces: principles, realizations, and applications. *Adv. Opt. Mater.* **6**, 1800415 (2018).
66. La Spada, L., Spooner, C., Haq, S. & Hao, Y. Curvilinear metasurfaces for surface wave manipulation. *Sci. Rep.* **9**, 3107 (2019).
67. Zuo, S. Y., Tian, Y., Wei, Q., Cheng, Y. & Liu, X. J. Acoustic analog computing based on a reflective metasurface with decoupled modulation of phase and amplitude. *J. Appl. Phys.* **123**, 091704 (2018).
68. Hwang, Y. & Davis, T. J. Optical metasurfaces for subwavelength difference operations. *Appl. Phys. Lett.* **109**, 181101 (2016).
69. Ozaktas, H. M. & Mendlovic, D. Fourier transforms of fractional order and their optical interpretation. *Opt. Commun.* **101**, 163–169 (1993).
70. Monticone, F., Estakhri, N. M. & Alù, A. Full control of nanoscale optical transmission with a composite metascreen. *Phys. Rev. Lett.* **110**, 203903 (2013).
71. Pors, A., Nielsen, M. G., Bozhevolnyi, S. I. Analog computing using reflective plasmonic metasurfaces. *Nano Lett.* **15**, 791–797 (2015).
72. Chizari, A., Abdollahramezani, S., Jamali, M. V. & Salehi, J. A. Analog optical computing based on a dielectric meta-reflector array. *Opt. Lett.* **41**, 3451–3454 (2016).
73. Zuo, S., Wei, Q., Tian, Y., Cheng, Y. & Liu, X. Acoustic analog computing system based on labyrinthine metasurfaces. *Sci. Rep.* **8**, 10103 (2018).
74. Zangeneh-Nejad, F. & Fleury, R. Performing mathematical operations using high-index acoustic metamaterials. *New J. Phys.* **20**, 073001 (2018).
75. Zangeneh-Nejad, F. & Fleury, R. Acoustic analogues of high-index optical waveguide devices. *Sci. Rep.* **8**, 10401 (2018).
76. Barrios, G. A., Retamal, J. C., Solano, E. & Sanz, M. Analog simulator of integro-differential equations with classical memristors. *Sci. Rep.* **9**, 12928 (2019).
77. Zhang, W., Qu, C. & Zhang, X. Solving constant-coefficient differential equations with dielectric metamaterials. *J. Opt.* **18**, 075102 (2016).
78. Zangeneh-Nejad, F. & Fleury, R. Acoustic rat-race coupler and its applications in non-reciprocal systems. *J. Acoust. Soc. Am.* **146**, 843–849 (2019).
79. Estakhri, N. M., Edwards, B. & Engheta, N. Inverse-designed metastructures that solve equations. *Science* **363**, 1333–1338 (2019).
80. Zangeneh-Nejad, F. & Fleury, R. Topological fano resonances. *Phys. Rev. Lett.* **122**, 014301 (2019).
81. Rechtsman, M. C. et al. Photonic Floquet topological insulators. *Nature* **496**, 196–200 (2013).
82. Bandres, M. A. et al. Topological insulator laser: experiments. *Science* **359**, eaar4005 (2018).
83. Xia, J. P. et al. Programmable coding acoustic topological insulator. *Adv. Mater.* **30**, 1805002 (2018).
84. Huber, S. D. Topological mechanics. *Nat. Phys.* **12**, 621–623 (2016).
85. Zangeneh-Nejad, F. & Fleury, R. Nonlinear second-order topological insulators. *Phys. Rev. Lett.* **123**, 053902 (2019).
86. Zangeneh-Nejad, F. & Fleury, R. Topological analog signal processing. *Nat. Commun.* **10**, 2058 (2019).
87. Xiao, Y. X., Ma, G., Zhang, Z. Q. & Chan, C. T. Topological subspace-induced bound state in the continuum. *Phys. Rev. Lett.* **118**, 166803 (2017).
88. Jalas, D. et al. What is — and what is not — an optical isolator. *Nat. Photonics* **7**, 579–582 (2013).
89. Zangeneh-Nejad, F. et al. Nonreciprocal manipulation of subwavelength fields in locally resonant metamaterial crystals. *IEEE Trans. Antennas Propag.* **68**, 1726–1732 (2019).
90. Zhang, W. & Zhang, X. Backscattering-immune computing of spatial differentiation by nonreciprocal plasmonics. *Phys. Rev. Appl.* **11**, 054033 (2019).
91. Alpaydin, E. *Introduction to Machine Learning* (MIT Press, 2020).
92. Beale, H. D., Demuth, H. B. & Hagan, M. T. *Neural Network Design* (PWS, 1996).
93. Orazbayev, B. & Fleury, R. Far-field subwavelength acoustic imaging by deep learning. *Phys. Rev. X* **10**, 031029 (2020).
94. Chakrabarti, A. Learning sensor multiplexing design through back-propagation. *Adv. Neural Inf. Process. Syst.* **29**, 3081–3089 (2016).
95. Horstmeyer, R., Chen, R. Y., Kappes, B. & Judkewitz, B. Convolutional neural networks that teach microscopes how to image. Preprint at [arXiv:1709.07223](https://arxiv.org/abs/1709.07223) (2017).
96. Lin, X. et al. All-optical machine learning using diffractive deep neural networks. *Science* **361**, 1004–1008 (2018).
97. Hunt, J. et al. Metamaterial apertures for computational imaging. *Science* **339**, 310–313 (2013).
98. Gollub, J. N. et al. Large metasurface aperture for millimeter wave computational imaging at the human-scale. *Sci. Rep.* **7**, 42650 (2017).
99. Sleasman, T., Imani, M. F., Gollub, J. N. & Smith, D. R. Dynamic metamaterial aperture for microwave imaging. *Appl. Phys. Lett.* **107**, 204104 (2015).
100. Sleasman, T. et al. Implementation and characterization of a two-dimensional printed circuit dynamic metasurface aperture for computational microwave imaging. Preprint at [arXiv:1911.08952](https://arxiv.org/abs/1911.08952) (2019).
101. Li, L. et al. Intelligent metasurface imager and recognizer. *Light Sci. Appl.* **8**, 97 (2019).
102. Li, L. et al. Machine-learning reprogrammable metasurface imager. *Nat. Commun.* **10**, 1082 (2019).
103. Liang, M., Li, Y., Meng, H., Neifeld, M. A. & Xin, H. Reconfigurable array design to realize principal component analysis (PCA)-based microwave compressive sensing imaging system. *IEEE Antennas Wirel. Propag. Lett.* **14**, 1039–1042 (2015).
104. del Hougne, P., Imani, M. F., Diebold, A. V., Horstmeyer, R. & Smith, D. R. Learned integrated sensing pipeline: Reconfigurable metasurface transceivers as trainable physical layer in an artificial neural network. *Adv. Sci.* **7**, 1901913 (2020).
105. Li, H. Y. et al. Intelligent electromagnetic sensing with learnable data acquisition and processing. *Patterns* **1**, 100006 (2020).
106. Shen, Y. et al. Deep learning with coherent nanophotonic circuits. *Nat. Photonics* **11**, 441–446 (2017).
107. del Hougne, P. & Leroose, G. Leveraging chaos for wave-based analog computation: Demonstration with indoor wireless communication signals. *Phys. Rev. X* **8**, 041037 (2018).
108. Matthes, M. W., del Hougne, P., de Rosny, J., Leroose, G. & Popoff, S. M. Optical complex media as universal reconfigurable linear operators. *Optica* **6**, 465–472 (2019).
109. Pierangeli, D., Marcucci, G. & Conti, C. Large-scale photonic Ising machine by spatial light modulation. *Phys. Rev. Lett.* **122**, 213902 (2019).
110. Abdolali, A., Momeni, A., Rajabaliapanah, H. & Achouri, K. Parallel integro-differential equation solving via multi-channel reciprocal bianisotropic metasurface augmented by normal susceptibilities. *New J. Phys.* **21**, 113048 (2019).
111. Wu, Y. et al. Arbitrary multi-way parallel mathematical operations based on planar discrete metamaterials. *Plasmonics* **13**, 599–607 (2018).

112. Momeni, A., Rajabali Panah, H., Abdolali, A. & Achouri, K. Generalized optical signal processing based on multioperator metasurfaces synthesized by susceptibility tensors. *Phys. Rev. Appl.* **11**, 064042 (2019).
113. Mosk, A. P., Lagendijk, A., Lerosey, G. & Fink, M. Controlling waves in space and time for imaging and focusing in complex media. *Nat. Photonics* **6**, 283–292 (2012).
114. Lee, P. A. & Fisher, D. S. Anderson localization in two dimensions. *Phys. Rev. Lett.* **47**, 882 (1981).
115. Titum, P., Lindner, N. H., Rechtsman, M. C. & Refael, G. Disorder-induced Floquet topological insulators. *Phys. Rev. Lett.* **114**, 056801 (2015).
116. Zangeneh-Nejad, F. & Fleury, R. Disorder-induced signal filtering with topological metamaterials. *Adv. Mater.* **32**, 2001034 (2020).
117. He, S. et al. Broadband optical fully differential operation based on the spin-orbit interaction of light. Preprint at *arXiv* <https://arxiv.org/abs/1910.09789> (2019).
118. He, S. et al. Spatial differential operation and edge detection based on the geometric spin Hall effect of light. *Opt. Lett.* **45**, 877–880 (2020).
119. Popa, B. I. & Cummer, S. A. Non-reciprocal and highly nonlinear active acoustic metamaterials. *Nat. Commun.* **5**, 3398 (2014).
120. Hess, O. et al. Active nanoplasmmonic metamaterials. *Nat. Mater.* **11**, 573–584 (2012).
121. Chen, K. et al. A reconfigurable active Huygens' metalens. *Adv. Mater.* **29**, 1606422 (2017).
122. Ghatak, A., Brandenburger, M., van Wezel, J. & Coulais, C. Observation of non-Hermitian topology and its bulk-edge correspondence. Preprint at *arXiv* <https://arxiv.org/abs/1907.11619> (2019).
123. Koutserimpas, T. T., Rivet, E., Lissek, H. & Fleury, R. Active acoustic resonators with reconfigurable resonance frequency, absorption, and bandwidth. *Phys. Rev. Appl.* **12**, 054064 (2019).
124. Zibar, D., Wymeersch, H. & Lyubomirsky, I. Machine learning under the spotlight. *Nat. Photonics* **11**, 749–751 (2017).
125. Zhou, H. et al. Self-learning photonic signal processor with an optical neural network chip. Preprint at *arXiv* <https://arxiv.org/abs/1902.07318v1> (2019).
126. Hughes, T. W., Williamson, I. A., Mirkov, M. & Fan, S. Wave physics as an analog recurrent neural network. *Sci. Adv.* **5**, eaay6946 (2019).
127. Tahersima, M. H. et al. Deep neural network inverse design of integrated photonic power splitters. *Sci. Rep.* **9**, 1368 (2019).
128. Yan, T. Fourier-space diffractive deep neural network. *Phys. Rev. Lett.* **123**, 023901 (2019).
129. Luo, Y. et al. Design of task-specific optical systems using broadband diffractive neural networks. *Light Sci. Appl.* **8**, 112 (2019).
130. Zhou, Y., Chen, R., Chen, W., Chen, R. P. & Ma, Y. Optical analog computing devices designed by deep neural network. *Opt. Commun.* **458**, 124674 (2020).
131. Guo, X., Lissek, H. & Fleury, R. Improving sound absorption through nonlinear active electroacoustic resonators. *Phys. Rev. Appl.* **13**, 014018 (2020).
132. Inagaki, T. et al. A coherent Ising machine for 2000-node optimization problems. *Science* **354**, 603–606 (2016).
133. Marandi, A., Wang, Z., Takata, K., Byer, R. L. & Yamamoto, Y. Network of time-multiplexed optical parametric oscillators as a coherent Ising machine. *Nat. Photonics* **8**, 937–942 (2014).
134. Yang, T. et al. All-optical differential equation solver with constant-coefficient tunable based on a single microring resonator. *Sci. Rep.* **4**, 5581 (2014).
135. MacLennan, B. J. A review of analog computing. *Univ. Tennessee* <https://library.eecs.utk.edu/pub/123> (2007).
136. de Solla Price, D. Gears from the Greeks. The mechanism: a calendar computer from ca. 80 BC. *Trans. Am. Philos. Soc.* **64**, 31–70 (1974).
137. Carr, B. Astronomical clocks: probing the early Universe with the millisecond pulsar. *Nature* **315**, 540 (1985).
138. Szalkai, I. General two-variable functions on the slide-rule. Preprint at *arXiv* <https://arxiv.org/abs/1612.03955> (2016).
139. Jenkins, H. V. An airflow planimeter for measuring the area of detached leaves. *Plant. Physiol.* **34**, 532–536 (1959).
140. Chapman, R. W. A simple form of tide predictor. *Nature* **68**, 322 (1903).
141. Lawshe, C. H. Jr. A nomograph for estimating the validity of test items. *J. Appl. Psychol.* **26**, 846–849 (1942).

**Acknowledgements**

R.F. and F.Z.-N. would like to acknowledge the support from the Swiss National Science Foundation, under grant number 172487. A.A. and D.L.S. acknowledge the support from the Air Force Office of Scientific Research, the Simons Foundation and the National Science Foundation. The authors acknowledge useful discussions with P. del Houge about machine-learning applications of computing metamaterials.

**Author contributions**

All authors contributed equally to writing the article.

**Competing interests**

The authors declare no competing interests.

**Publisher's note**

Springer Nature remains neutral with regard to jurisdictional claims in published maps and institutional affiliations.

© Springer Nature Limited 2020